JGR Space Physics

RESEARCH ARTICLE
10.1029/2023JA031350

Special Section:
Fifteen Years of THEMIS Mission

Contribution of Kinetic Alfvén Waves to Energetic Electron Precipitation From the Plasma Sheet During a Substorm

Yangyang Shen[1], Anton V. Artemyev[1,2], Xiao-Jia Zhang[1,3], Ying Zou[4], Vassilis Angelopoulos[1], Ivan Vasko[2,5], Andrei Runov[1], Ethan Tsai[1], and Colin Wilkins[1]

[1]Department of Earth, Planetary, and Space Sciences, University of California, Los Angeles, CA, USA, [2]Space Research Institute of Russian Academy of Sciences, Russia, Moscow, [3]Department of Physics, University of Texas at Dallas, Richardson, TX, USA, [4]The Center for Space Plasma and Aeronomic Research, University of Alabama, Huntsville, AL, USA, [5]Space Science Laboratory, University of California, Berkeley, CA, USA

Abstract Energetic ($\gtrsim$50 keV) electron precipitation from the magnetosphere to the ionosphere during substorms can be important for magnetosphere-ionosphere coupling. Using conjugate observations between the THEMIS, ELFIN, and DMSP spacecraft during a substorm, we have analyzed the energetic electron precipitation, the magnetospheric injection, and the associated plasma waves to examine the role of waves in pitch-angle scattering plasma sheet electrons into the loss cone. During the substorm expansion phase, ELFIN-A observed 50–300 keV electron precipitation from the plasma sheet that was likely driven by wave-particle interactions. The identification of the low-altitude extent of the plasma sheet from ELFIN is aided by DMSP global auroral images. Combining quasi-linear theory, numerical test particle simulations, and equatorial THEMIS measurements of particles and fields, we have evaluated the relative importance of kinetic Alfvén waves (KAWs) and whistler-mode waves in driving the observed precipitation. We find that the KAW-driven bounce-averaged pitch-angle diffusion coefficients $D_{\alpha_0\alpha_0}$ near the edge of the loss cone are $\sim 10^{-6}$–10^{-5} s^{-1} for these energetic electrons. The $D_{\alpha_0\alpha_0}$ due to parallel whistler-mode waves, observed at THEMIS ~10-min after the ELFIN observations, are $\sim 10^{-8}$–10^{-6} s^{-1}. Thus, at least in this case, the observed KAWs dominate over the observed whistler-mode waves in the scattering and precipitation of energetic plasma sheet electrons during the substorm injection.

Plain Language Summary One of the key elements of magnetosphere-ionosphere coupling is energetic electron precipitation from the magnetosphere to the ionosphere. This precipitation becomes particularly significant and geoeffective during substorms, when it can cause radio transmission interference by increasing ionospheric radio absorption. Understanding the mechanisms of such precipitation is thus critical to space weather nowcasting and forecasting. In this paper, using magnetically conjugate observations between the THEMIS, ELFIN, and DMSP satellites in both the Earth's magnetosphere and ionosphere, and aided with numerical simulations and theoretical estimates, we examine the relative importance of different plasma waves in the scattering and precipitation of energetic electrons from the plasma sheet during a substorm. By comparing the electron scattering efficiencies due to the observed kinetic Alfvén waves (KAWs) and whistler-mode waves, we conclude that KAWs dominate over whistler-mode waves, at least in this case, in driving the observed energetic (50–300 keV) electron precipitation by ELFIN during the substorm expansion. Thus, the KAW may be an important, previously overlooked contributor to energetic electron precipitation from the plasma sheet during substorms.

Key Points:

- Conjugate spacecraft observations allow evaluating the relative importance of kinetic Alfvén waves (KAWs) and whistlers in driving energetic electron precipitation
- KAW-driven electron bounce-averaged diffusion rates above 50 keV are one order of magnitude larger than those due to whistler-mode waves
- KAWs can contribute to and may dominate the scattering and precipitation of energetic electrons from the substorm plasma sheet

Supporting Information:

Supporting Information may be found in the online version of this article.

Correspondence to:

Y. Shen,
yshen@epss.ucla.edu

Citation:

Shen, Y., Artemyev, A. V., Zhang, X.-J., Zou, Y., Angelopoulos, V., Vasko, I., et al. (2023). Contribution of kinetic Alfvén waves to energetic electron precipitation from the plasma sheet during a substorm. *Journal of Geophysical Research: Space Physics*, *128*, e2023JA031350. https://doi.org/10.1029/2023JA031350

Received 26 JAN 2023
Accepted 28 MAR 2023

1. Introduction

The magnetospheric substorm (Akasofu, 1964; Angelopoulos et al., 2013) is an important geophysical process that powers dynamic auroras (Kataoka et al., 2021) and energizes the radiation belts (Mauk et al., 2013). In the magnetotail, a substorm is often accompanied by transient, meso-scale structures evidenced as ion bursty bulk flows (Angelopoulos et al., 1992; Baumjohann et al., 1990), plasma injections (Birn et al., 2013; Gabrielse et al., 2014; McIlwain, 1974), and dipolarizing flux bundles (DFBs) (Liu et al., 2014; Runov et al., 2009), which occur on time scales of minutes and with dawn-dusk extent of the order of 1–3 R_E (Nakamura et al., 2004; Runov et al., 2011; Sitnov et al., 2019). Plasma injections are often observed to propagate earthward with electron flux increases in the energy range of tens to hundreds of keV at the nightside magnetotail-inner magnetosphere interface (Birn et al., 1998; Gabrielse et al., 2014; Turner et al., 2016; Ukhorskiy et al., 2022). The

energetic electrons within the injection region and near the DFB exhibit complex, energy-dependent anisotropic distributions, such as pancake (peaking at 90°) or cigar-shaped (peaking at 0° and 180°) (Fu et al., 2011; Runov et al., 2013; X. Zhou et al., 2010). These anisotropic electrons have been explained by both adiabatic and non-adiabatic acceleration mechanisms (Birn et al., 2014; Deng et al., 2010; Gabrielse et al., 2017; Khotyaintsev et al., 2011; Sorathia et al., 2018). The buildup of such anisotropy during these structures must necessarily be limited by wave-particle interactions (see discussions in X. Zhang et al. (2018) and Ukhorskiy et al. (2022)). The waves excited by excessive anisotropy, both suppress the anisotropy and can cause electron pitch-angle scattering into the loss cone and precipitation to the ionosphere at some other energy range. Such precipitation plays a critical role in magnetosphere-ionosphere coupling (Kepko et al., 2014; Khazanov et al., 2018; Ni et al., 2016; Nishimura et al., 2020). Lower-energy ($\lesssim$50 keV) electron precipitation generates the diffuse aurora (Ni et al., 2016; Ni, Thorne, Meredith, et al., 2011; Shen et al., 2021; Thorne et al., 2010; X. Zhang et al., 2014) and higher-energy electron precipitation increases ionospheric radio signal absorption (e.g., Hargreaves, 1969; Kellerman et al., 2015; Spanswick et al., 2010).

By analyzing auroral riometer absorption data collected from 60 substorm events as recorded across 40 stations, Berkey et al. (1974) found that the auroral absorption moved both eastward and westward, representing dynamic motion of ∼50–300 keV electron precipitation. The precipitation region expands both equatorward and poleward from the initiation region and is primarily confined to the auroral zone latitudes. A similar pattern of substorm energetic precipitation expansion within $4 < L < 12.5$ has been reported by Clilverd et al. (2012) using VLF radio signal phase observations and riometer measurements. Gabrielse et al. (2019) has recently combined THEMIS in-situ measurements, ground-based all-sky images, and riometer absorption data to study the movement of substorm electron injections and the associated energetic electron precipitation. They suggested that a series of small-scale DFBs and plasma injections can accumulate near the Earth to build up large-scale injections in the flux pileup region (∼6–∼10 R_E wide), which could expand even further azimuthally (mostly westward) and also tailward. During cases of prolonged activity, DFBs may rebound and oscillate near the equator (Panov et al., 2010; Schmid et al., 2011). These observations of rebounding and often vortical flows could reconcile the discrepancies in previous in-situ and ground-based observations of the movements of substorm injection and energetic precipitation (see discussion in Spanswick et al. (2010) and Gabrielse et al. (2019)). Prior works have suggested that wave-particle interactions are necessary to explain the ground-based riometer signals during a substorm (Baker et al., 1981; Gabrielse et al., 2019; Lam et al., 2010; Spanswick et al., 2007). However, the specific wave modes and scattering mechanisms implicated in the driving of the energetic precipitation from plasma sheet electron injections are not well understood.

Various kinetic wave structures have been previously associated with substorm magnetic field dipolarizations and plasma injections. Deng et al. (2010) have shown that DFBs are associated with both whistler-mode chorus waves (Tsurutani & Smith, 1974) and time domain structures (TDSs), the latter appearing as broadband electrostatic waves (Mozer et al., 2015). Chorus waves are usually observed within the DFB itself or behind it (Breuillard et al., 2016; Khotyaintsev et al., 2011; Viberg et al., 2014). There, the electron perpendicular anisotropy has been shown to drive the whistler-mode wave unstable (W. Li et al., 2009; X. Zhang et al., 2018, 2019). Similarly, electron cyclotron harmonic (ECH) waves were found to often coincide with or follow substorm injections (71%) and DFBs (52%) (X. Zhang & Angelopoulos, 2014). Whistler-mode waves, ECH waves, and TDSs are typically associated with low-energy (<∼50 keV) electron precipitation to the diffuse aurora from the plasma sheet (e.g., Ni et al., 2016; Shen et al., 2020; Vasko et al., 2018). Although whistler-mode chorus waves have been known to accelerate and scatter energetic (>50 keV) electrons from the inner magnetosphere ($L \leq 7$) (see reviews by Shprits et al. (2008), Thorne (2010), Millan and Baker (2012), Artemyev et al. (2016), and Thorne et al. (2021)), their scattering efficiency drops significantly as the energy of the plasma sheet electrons increases from 10 to 50–100 keV (Ghaffari et al., 2020; Ni et al., 2016; Ni, Thorne, Meredith, et al., 2011; Ni, Thorne, Shprits, et al., 2011).

In addition, lower-hybrid waves with frequencies near and above the lower-hybrid frequency have also been detected near the boundaries of the DFBs, known as dipolarization fronts (DFs) (Graham et al., 2017; Norgren et al., 2012; V. A. Sergeev et al., 2009; M. Zhou et al., 2009). These waves are important for plasma acceleration and heating (Cairns & McMillan, 2005; Divin et al., 2015; Drake et al., 2003), but they are incapable of scattering electrons into the loss cone. Furthermore, M. Zhou et al. (2014) have shown observations of large-amplitude (∼2 nT) low-frequency (sub-Hz on the order of f_{ci}) magnetosonic waves associated with DFs. Magnetosonic waves can scatter electrons at intermediate (∼10°–∼70°) pitch angles but are also ineffective in scattering electrons into

the loss cone (e.g., Ma et al., 2016; Mourenas et al., 2013; M. Zhou et al., 2014). Moreover, ultra-low-frequency (ULF) waves, which are on MHD scales, also play a critical role in the substorm dipolarization processes (e.g., Liu et al., 2017; Shiokawa et al., 1997), but they seldom contribute to electron pitch-angle scattering directly (Ukhorskiy & Sitnov, 2013; X.-J. Zhang et al., 2019). Electromagnetic ion cyclotron (EMIC) waves have been sporadically observed in the midnight plasma sheet (Wang et al., 2017), and they primarily scatter relativistic (~MeV) electrons (e.g., Albert, 2003; Ni et al., 2015; Summers & Thorne, 2003).

The kinetic Alfvén wave (KAW) is also a common and powerful wave mode associated with substorm injections and DFBs. KAWs are quasi-electrostatic waves with perpendicular wavelengths comparable to the local ion gyroradius (Hasegawa & Chen, 1975). They have been observed in the plasma sheet both at high latitudes and close to the equator (Angelopoulos et al., 2002; Deng et al., 2010; Wygant et al., 2002), usually in correlation with braking ion bursty bulk flows (Angelopoulos et al., 2002; Chaston et al., 2012; Ergun et al., 2015). Poynting flux carried by KAWs can be an important carrier of energy transfer from plasma sheet ion kinetic energy to electromagnetic energy flowing into the ionosphere at high-latitudes (Angelopoulos et al., 2002; Chaston et al., 2012; Keiling, 2009). KAWs in the plasma frame appear as broadband waves in the spacecraft frame, in the presence of fast ion flows (Chaston et al., 2012). Using statistics of >170 events from THEMIS in the outer magnetosphere ($L \geq 8$), Ergun et al. (2015) demonstrated a good correlation between large-amplitude (>50 mV/m) KAWs and fast ion flows (>100 km/s in 85% of the events), as well as DFBs (in 91% of the events). The events were primarily in the pre-midnight sector (as is typical of fast flows and DFBs). A similar correlation between KAWs and plasma injection boundaries has also been reported in the inner magnetosphere by Malaspina et al. (2015) using Van Allen Probe observations. They also showed that KAW broadband emissions were comoving with the injections. A recent statistical study from Usanova and Ergun (2022) in the flow-braking region has suggested that large-amplitude electric fields (which we believe could be potentially comprised of KAWs), may be responsible for local acceleration and heating of energetic electrons (Ergun et al., 2022), so as to supply a seed population for the outer radiation belt (Jaynes et al., 2015). It is thus critically important to understand the role KAWs play in plasma sheet injections and magnetic field dipolarizations, in particular during substorms, and whether they can contribute to energetic injection electron scattering or acceleration.

It has only recently been recognized (Shen et al., 2022a; Shen et al., 2022c) that KAWs can resonantly scatter energetic injection electrons with energies of tens to hundreds of keV through Doppler-shifted Landau resonance. This resonant interaction results from coupling between KAW electric fields and electron perpendicular guiding-center drifts at magnetic field gradients. By comparing conjugate observations from the MMS and ELFIN spacecraft with test particle simulation results, Shen et al. (2022c) have provided preliminary evidence that KAWs may contribute to energetic electron precipitation from a plasma sheet injection. However, the relative role of KAWs and other scattering mechanisms in driving energetic precipitation has not been addressed yet. Here we address this issue using observations from the ELFIN, DMSP, and THEMIS missions, which provide approximately conjugate measurements from the vantage points of both the ionosphere and the equatorial magnetosphere during a substorm event.

2. Instrumentation and Data

We use data from the three THEMIS spacecraft (A, D, and E) (Angelopoulos, 2008) in the magnetotail (at ~11R_E) spanning the period of 01:00–02:10 UT during a substorm event on 10 July 2021. From each THEMIS spacecraft we use injection electron fluxes from 25 to 900 keV measured by the Solid State Telecope (SST) instrument (Angelopoulos, Sibeck, et al., 2008; Runov et al., 2015), DC vector magnetic field at spin resolution (~3 s for the *fgs* data set) measured by the Fluxgate Magnetometers (FGM) (Auster et al., 2008), electric and magnetic field wave power spectra with frequencies up to 4 kHz (FFF spectra every ~1 s), particle burst waveform data at 512 sps (DC-coupled), and short-burst (~5 s) waveform data 16,384 sps (AC-coupled), measured by the Electric Field Instrument (EFI), the search coil magnetometer (SCM), and the Digital Fields Board (DFB) (Bonnell et al., 2008; Cully et al., 2008; Le Contel et al., 2008). In addition, background electron densities are inferred from spacecraft potentials (Bonnell et al., 2008), and electron and ion temperatures are obtained from thermal (≲30 keV) and high-energy (~25–900 keV) measurements by the Electrostatic Analyzers (ESA) (McFadden et al., 2008) and the SST instrument.

We also use energetic electron measurements from the ELFIN twin CubeSats (ELFIN-A, ELFIN-B; or ELA, ELB) (Angelopoulos, Tsai, et al., 2020), which were roughly magnetically conjugate with THEMIS during

the growth phase of a substorm near 01:06–01:10 UT (ELFIN-A) and during the expansion phase of the same substorm near 01:31–01:35 UT (ELFIN-B). Mounted on the spinning ELFIN CubeSats, flying on polar circular orbits at ∼450 km altitude, the energetic particle detector for electrons (EPDE) instrument measures electrons from 50 keV to ∼6 MeV in 16 energy channels, and pitch-angle distributions in 16 (full-spin) angular sectors with a resolution (FWHM) of ∼22.5° every 3 s. The **B** field is within ±15° of the spin plane, allowing ELFIN to reliably resolve the local ionospheric loss cone (∼67°) and separate precipitating, backscattered, and trapped electron fluxes (see Angelopoulos et al., 2022). Multiple energy channels with fine energy step size and full pitch-angle resolution allow us to distinguish between wave-particle interactions and field-line curvature scattering based on the characteristic precipitation signatures of these processes in energy and pitch-angle (V. A. Sergeev et al., 2018; Shen et al., 2022c).

In addition, we use observations from the DMSP spacecraft (F17 and F18) to reveal the substorm-related auroral activities as well as the associated low-energy electron precipitation and magnetic field measurements at an altitude of ∼840 km. The optical auroral emissions demarcate the auroral boundaries or the plasma sheet boundaries providing context to ELFIN's ionospheric measurements. These optical measurements also support the origin of energetic precipitation measured by ELFIN from the magnetospheric plasma sheet. The DMSP Special Sensor Ultraviolet Spectrographic Imager (SSUSI) instrument provides far ultraviolet (FUV) auroral imagery covering a wavelength range of 110–180 nm, which is divided into Lyman-Birge-Hopfield short (LBHS) within 110–160 nm wavelengths and Lyman-Birge-Hopfield long (LBHL) within 160–180 nm wavelengths (Paxton et al., 2002; Sotirelis et al., 2013). We will use the LBHL measurements in horizon-to-horizon cross-track scanning mode accumulated over the two conjugate (with ELFIN and THEMIS) auroral oval passages during 01:00–01:21 UT and 01:55–02:15 UT. The SSJ5 particle detector measures fluxes of ions and electrons from 30 eV to 30 keV once per second (Hardy et al., 1984). We also use magnetic field data from the Special Sensor Magnetometer (SSM) instrument (Rich et al., 1985) and electron densities from the Special Sensor Ions, Electrons, and Scintillation (SSIES) instrument. Lastly, we use the *SML* index (the generalization of *AL*) to support our identification of substorm activities (Gjerloev, 2012; Newell & Gjerloev, 2011).

3. Overview of the Event on 10 July 2021

Figure 1 shows an overview of the THEMIS-ELFIN conjunction event (Panel (a)) on 10 July 2021, when THEMIS observed energetic electron injection, magnetic fields, ion flows, and plasma waves in the equatorial plasma sheet (Panel (b)) and the two ELFIN CubeSats observed energetic (>50 keV) electron precipitation in the southern auroral ionosphere (ELFIN-B: Panel (c) and ELFIN-A: Panel (d)). Figure 1a shows the magnetic conjunction of the three THEMIS spacecraft in the magnetotail magnetic field during the period of 01:20–01:30 UT. Because THEMIS-A and THEMIS-E have very similar observations to THEMIS-D, all located south of the neutral sheet near magnetic midnight (*MLT* ∼ 23.7 hr), we mostly discuss observations from THEMIS-D here.

Figure 1b shows that the absolute value of SML index was relatively stable around 70 nT prior to ∼01:26:40 UT, when SML increased suddenly and progressively to more than 300 nT, signifying the initiation of a magnetospheric substorm expansion. The THEMIS spacecraft first observed current-sheet thinning with increasing $|B_x|$ and decreasing B_z during the substorm growth phase, before they encountered the dipolarizing flux bundles (DFBs) around 01:26:40 UT. All THEMIS spacecraft entered the plasma sheet proper near 01:28 UT, with $|B_x/B_{lobe}| < 0.3$. Assuming pressure balance in the z direction, the lobe field $B_{lobe} = \sqrt{2\mu_0 P_{tot}}$ and P_{tot} is the total pressure containing only B_x and B_y components. Here the condition $|B_x/B_{lobe}| < 0.3$ is used as a proxy to indicate that the spacecraft observations are in the central plasma sheet (Liu et al., 2013). Near 01:26:40 UT, a sharp increase of particle fluxes (seventh panel from top), along with multiple DFBs, intense Alfvénic broadband waves and ion bursty bulk flows (BBFs), engulfed the spacecraft and was sustained almost an hour. Multiple DFBs were observed, having peaks in B_z up to ∼20 nT with magnetic field elevation angle increases of more than 30°. Coinciding with the substorm expansion onset and in the few-minute period after (01:27 - 01:32 UT), earthward ion flows V_x exceeded 500 km/s, oscillating in correlation with the magnetic perturbations, suggesting the presence of compressional ULF waves (Kepko et al., 2014; Runov et al., 2014; Shiokawa et al., 1997) and significant magnetic flux transport $-V_x \times B$ (e.g., Liu et al., 2014) from the reconnection site (Angelopoulos, Artemyev, et al., 2020; Angelopoulos, McFadden, et al., 2008). The injected electrons had maximum energies of >500 keV and the broadband low-frequency (1–60 Hz) waves had a mean absolute electric field amplitude of >10 mV/m. As will be demonstrated later, the broadband waves in the beginning of the injection near 01:27–01:31 UT consist

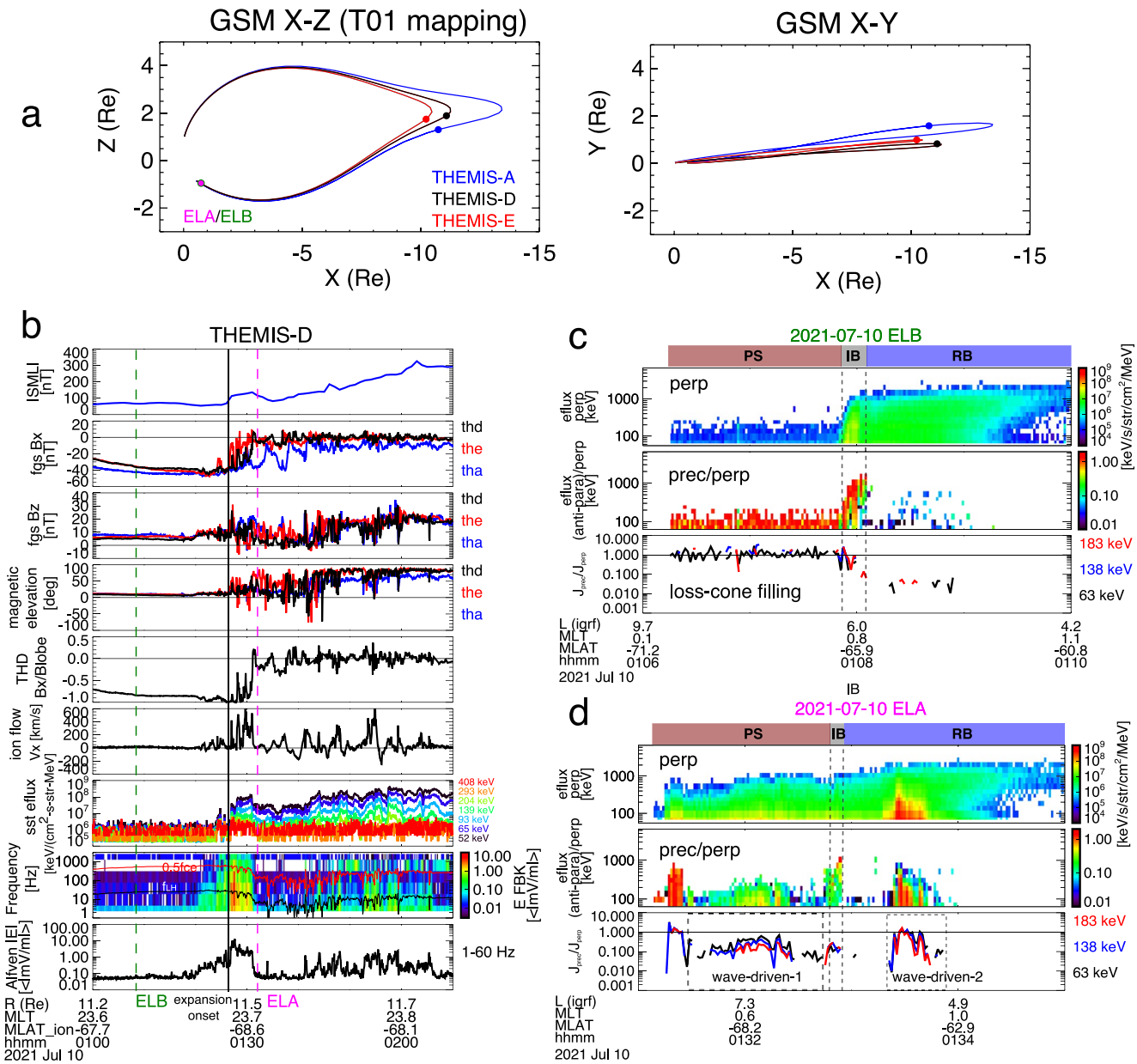

Figure 1. THEMIS-ELFIN conjugate observations of a substorm injection and energetic electron precipitation on 10 July 2021. (a) THEMIS and ELFIN positions in GSM *X*-*Z* and *X*-*Y* projections. Magnetic field line tracing is performed using the T01 model (Tsyganenko, 2002). (b) Panels from top to bottom: the absolute *SML* index; THEMIS A, D, and E magnetic field B_x in GSM; magnetic field B_z; magnetic field elevation angle $\theta_{DF} = \arctan\left(B_z/\sqrt{B_x^2 + B_y^2}\right)$; THEMIS-D B_x/B_{lobe}; THEMIS-D ion flow velocities V_x in GSM; THEMIS-D SST electron energy flux within 50–500 keV; THEMIS-D filter-bank (FBK) electric field spectra; integrated FBK wave electric field within 1–60 Hz, calculated as $|E| = \sqrt{\sum_f \langle |E_w(f)| \rangle^2 \pi^2/8}$, where $\langle |E_w(f)| \rangle$ is the FBK mean absolute wave amplitude. Note that the magnetic latitudes (MLAT) are calculated at the ionospheric footprints (~110 km) in (Altitude-adjusted corrected geomagnetic) AACGM coordinates. (c) ELFIN-B (ELB) substorm growth-phase observations of near-perpendicular electron energy fluxes, along with the loss cone filling ratios (flux ratios) J_{prec}/J_{perp} spectrogram and line plots for 63, 138, and 183 keV. (d) ELFIN-A (ELA) substorm expansion-phase observations of near-perpendicular electron fluxes and loss cone filling ratios spectrogram and line plots in the same format as in (c). The isotropy boundary (or the inner edge of the plama sheet) is indicated in between the gray dashed lines, and two wave-driven precipitation regions are indicated by the rectangular boxes. Note that the conjunction time stamps of ELA and ELB with THEMIS are highlighted in (b) with vertical dashed lines.

mainly of KAWs and time domain structures (TDSs) (Mozer et al., 2015; Shen et al., 2021), whereas after 01:40 UT there exist additionally, lower-hybrid (LH) waves (Deng et al., 2010; Graham et al., 2017), whistler-mode waves (X. Zhang et al., 2018), and electron cyclotron harmonic (ECH) waves (X. Zhang & Angelopoulos, 2014).

Simultaneously with the commencement of the injection near 01:26:40 UT, B_x and ion flows V_x were observed to periodically oscillate, indicating flapping motion of the plasma sheet (e.g., V. Sergeev et al., 2003).

In association with THEMIS observations from the plasma sheet, the two ELFIN spacecraft in the southern ionosphere observed significant energetic electron precipitation (Figures 1c and 1d). ELFIN-B and -A, in that sequence, traversed the auroral latitudes (~−65°–~−72°) during the growth phase and the expansion phase, respectively, both at *MLT* ~0.1–0.8 hr. ELFIN-B's crossing occurred near 01:06 UT, before the injection at THEMIS, whereas ELFIN-A's was concurrent with the injection, near 01:32 UT. Although known to be somewhat inaccurate (the uncertainty reaches 3° in latitude during active times), magnetic mapping of THEMIS and ELFIN to the ionosphere (~110 km) is performed to demonstrate the closeness of the ELFIN satellites to the THEMIS footpoints at least in *MLT*, and the relation of both missions' magnetic projections to the large-scale auroral region. For our mapping we used the T01 model (Tsyganenko, 2002) with real-time, lag-compensated input parameters of the *Dst* index (~12 nT), the IMF B_y (~−2 nT) and B_z (~−6 nT), and the solar wind density (~16 cm^{-3}) and speed (~350 km/s).

While ELFIN-B only observed weak and isotropic precipitation poleward of the isotropy boundary (IB, as characterized by a latitudinal boundary of isotropic fluxes at energies that dispersively decrease with increasing latitude; see V. A. Sergeev et al. (1993, 2012) for details and references), ELFIN-A observed intense, anisotropic electron precipitation from the plasma sheet region (PS), where electrons were energized and their fluxes enhanced during the substorm expansion phase. It is worth emphasizing here that the contribution of atmospheric backscattered electron fluxes has been excluded from the precipitation energy fluxes when calculating J_{prec}/J_{perp} (J_{prec} is the precipitating flux and J_{perp} is the perpendicular flux) ratios in Figures 1c and 1d (see, e.g., Mourenas et al., 2021).

The plasma sheet precipitation observed at ELFIN-A (during substorm expansion) is dominated by energies below ~300 keV, except for a couple of transient precipitation intervals when precipitation exceeds 500 keV. That electron energies of significant flux in the plasma sheet can be > 300 keV and exceed 500 keV has also been reported by previous missions in the magnetotail (Christon et al., 1991; Sarafopoulos et al., 2001; Sarris et al., 1976). Nonetheless, the typical plasma sheet precipitation region is identified from ELFIN based on: (**a**) significant near-perpendicular (bounce-trapped) fluxes are observed poleward of the IB (V. A. Sergeev et al., 1993); (**b**) significant down-going (precipitating) fluxes are observed at $L_{IGRF} > 7$ with energies below ~300 keV; and (**c**) the precipitation region is within the main auroral oval as observed by DMSP (and will be discussed below).

During the growth phase (Figure 1c), the weak isotropic electron precipitation at ELFIN-B poleward of the IB is caused by field-line curvature (FLC) scattering of plasma sheet electrons due to the current sheet thinning process (McPherron, 1972; V. A. Sergeev & Tsyganenko, 1982; V. A. Sergeev et al., 1983). During the expansion phase, dipolarized magnetic fields will increase the curvature radius and reduce FLC-scattering. This explains the observation of mostly anisotropic precipitation from the plasma sheet at ELFIN-A (in Figure 1d). Note that localized, isotropic precipitation with energies of over ~500 keV was observed at the poleward boundary of the plasma sheet, likely associated with localized current sheet/FLC-scattering. The anisotropic precipitation observed near 01:32 UT shows higher loss cone filling ratios for lower-energy electrons, as indicated by the flux ratios J_{prec}/J_{perp} in the third panel of Figure 1d. These ratios suggest that scattering and loss is more efficient for lower-energy electrons than for higher-energy electrons.

This energy dependence of the precipitating-to-perpendicular anisotropy ratio cannot be explained by FLC-scattering, which would produce more efficient higher-energy electron precipitation than lower-energy precipitation, due to decreasing curvature-radius-to-gyroradius ratios with increasing energy (Buchner & Zelenyi, 1989; Delcourt et al., 1994; V. A. Sergeev et al., 1983). It is very likely that this energy dependence is caused by wave scattering, which can produce more efficient electron scattering at lower energies (Ni et al., 2016; Shen et al., 2022a; Summers et al., 2007). A similar, wave-driven precipitation region can be identified at 01:33:30 UT except that it is located within the outer radiation belt (RB), since the *L*-shell around that time is low (~5) and the precipitation is embedded in a prolonged interval of high perpendicular fluxes exceeding 500 keV. It is likely that whistler-mode waves, which are routinely observed in the outer radiation belt, can account for the broadband precipitation with energies from ~50 to more than 500 keV and have been studied extensively in the past (e.g., Millan & Thorne, 2007; Shprits et al., 2008; Thorne, 2010; Thorne et al., 2021, and references therein).

To confirm that the injection near the equator observed by THEMIS-D is related to the aforementioned wave-driven precipitation event observed at ELFIN-A, we compare in Figure 2 the energy-spectrum of the

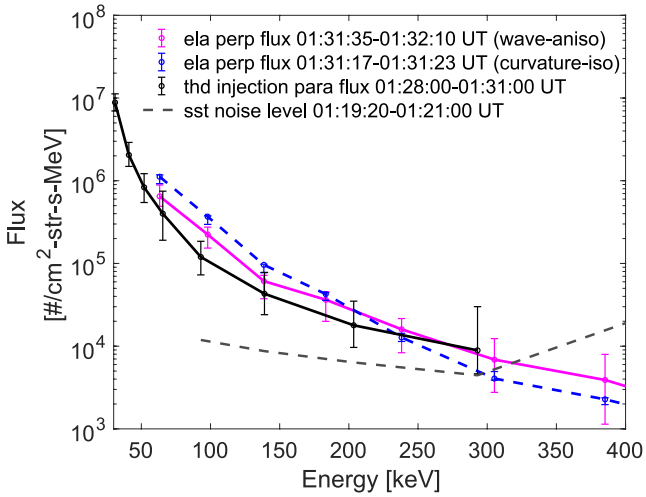

Figure 2. Comparison of differential number flux energy-spectra measured by THEMIS-D during injection periods (solid black line, 01:28:00–01:31:00 UT, see Figure 1b), by ELFIN-A within the ionospheric wave-driven, anisotropic precipitation region (solid magneta line, 01:31:35–01:32:10 UT, see wave-driven-1 in Figure 1d), and by EFLIN-A near the poleward boundary of the auroral precipitation region (dashed blue line, 01:31:17–01:32:23 UT, see Figure 1d). Median values of the spectra are shown along with errorbars. The gray-dashed line indicates the noise-level spectrum obtained from the time period of 01:19:20–01:21:00 UT during the growth phase, when no significant energetic injection fluxes were observed. Note that the noise level of median flux spectra from THEMIS-D SST becomes higher than or comparable with the measured injection fluxes at energies larger than ∼300 keV. Thus, SST flux enhancements at >∼300 keV cannot be interpreted as of physical origin and we do not show spectra at these higher energies.

parallel-to-**B** differential number flux (pitch angles less than 22.5° from the field line) at THEMIS-D (black solid line) with the perpendicular number flux energy-spectrum measured at ELFIN-A (magneta solid line). Assuming adiabatic motion of energetic electrons, perpendicular electrons measured at ELFIN-A would have an equatorial pitch angle of ∼2°. As demonstrated by Artemyev et al. (2022), flux distributions measured by ELFIN and THEMIS are comparable if the regions where the spacecraft reside in the ionosphere and magnetosphere are approximately magnetically conjugate. Indeed, nearly identical spectra are observed at THEMIS-D during the injection period (01:28–01:31 UT) and at ELFIN-A within the wave-driven, anisotropic precipitation period (01:31:35–01:32:10 UT) (see Figure 1d). The distributions are considered nearly identical because the spectra overlap within the errorbars at all comparable energies. Conversely, the ELFIN spectra measured during the intense precipitation region (01:31:17–01:31:23 UT) just poleward of the wave-driven precipitation in Figure 1d (blue dashed line in Figure 2) is significantly different from the THEMIS-D injection spectrum (black line in same figure), particularly at energies below ∼150 keV. We conclude that the plasma sheet injection fluxes neasured by THEMIS-D during 01:28–01:31 UT are likely associated with the wave-driven, anisotropic precipitation at ELFIN-A around 01:32 UT.

Two DMSP spacecraft, F17 and F18, were in conjunction with ELFIN during this event. They provided additional support that the energetic electron precipitation at ELFIN was probably due to fluxes from the plasma sheet (which THEMIS was observing in situ at the time). Figure 3 shows DMSP FUV auroral images in the LBHL band (160–180 nm), plasma densities, magnetic perturbations, and low-energy (<30 keV) particle precipitation energy fluxes. These measurements were taken first by F18 and next by F17 as they traversed the aurora in the southern ionosphere during the substorm growth phase (01:00–01:15 UT) and expansion phase (01:55–02:15 UT), respectively. The ionospheric footprints of ELFIN-A, ELFIN-B, THEMIS, and DMSP are highlighted on the images in Figures 3b and 3e. They reveal that at the times of interest both F18 and F17 were within the auroral oval at high latitudes, near the magnetic midnight meridian. It is worth noting that we do not imply that THEMIS and ELFIN are exactly conjugate along the same field line. We merely suggest that they are sufficiently close, and that the plasma and field characteristics of the ELFIN's equatorial source region and those at the THEMIS are similar.

During the growth phase, the FUV image in Figure 3a reveals two distinct bright latitudinal bands one at low and one at high latitudes bracketing the auroral oval. The equatorward band is likely the thin growth-phase arc, typical during substorms. It is in the vicinity of the IB precipitation as identified from ELFIN-B near 01:08 UT (Figure 1c). When DMSP F18 traversed the plasma sheet equatorward boundaries, once near 01:05 UT in the premidnight sectors and once 01:12 UT in the postmidnight sectors, SSJ5 measured energetic electron precipitation of >10 keV, which coincided with energy-dispersed ions with energies surpassing the instrument energy limit of 30 keV. These features, along with the sharp drop-off of the electron energies at the equatorward sides of the auroral precipitation region, are consistent with previous observations of the inner edge of the plasma sheet (Elphic et al., 1999). The poleward bright latitudinal band is at the same latitude as the low-energy (< a few keV) precipitation in Figure 3c. It is likely related to Alfvén wave acceleration, typically observed in the high-latitude auroral region, and has been extensively studied (e.g., Liang et al., 2019).

During the expansion phase, DMSP F17 measured an enlarged auroral oval (Figure 3d) and observed various dynamic auroral forms near midnight, such as the poleward boundary intensification, bifurcations and north-south-aligned aurora streamers (e.g., Forsyth et al., 2020; Henderson, 2012; Lyons et al., 2012; Nishimura et al., 2011). Importantly, most of the energetic electron precipitation measured by ELFIN-A during the period of 01:31–01:34 UT is within the auroral precipitation region as evidenced by the DMSP auroral image. The uncertainty of field-line tracing of ELFIN and DMSP to the ionosphere is less than 0.5° in latitude, because the two missions have low-altitude orbits (∼450 km and ∼840 km, respectively) where the background magnetic field

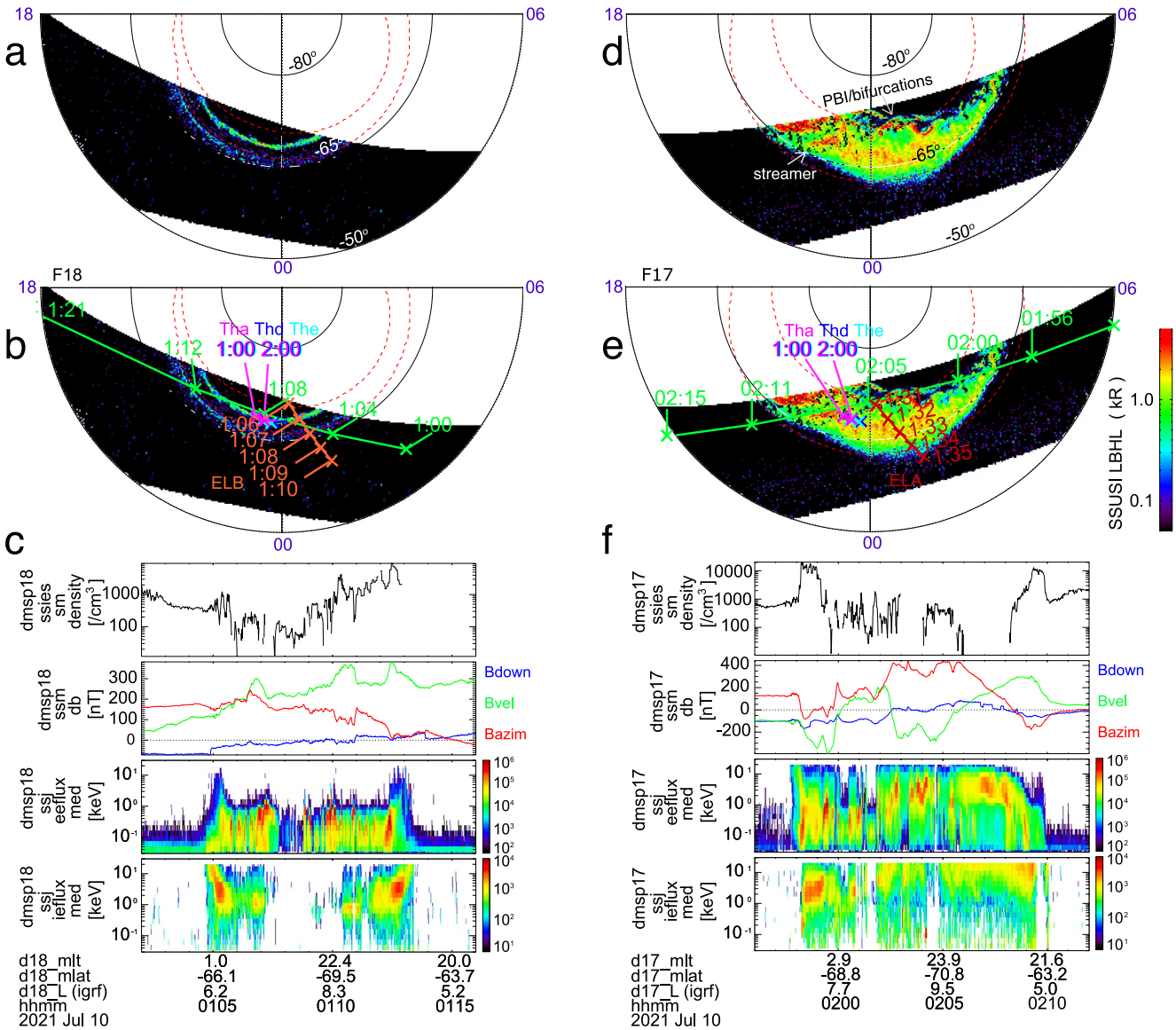

Figure 3. Overview of DMSP F18 and F17 observations during the periods of 01:00–01:15 UT and 01:55–02:15 UT (a and d) FUV auroral images measured by F18 (left) and F17 (right) during the growth and expansion phases of the substorm, respectively. The dashed circles delineate roughly the auroral oval poleward and equatorward boundaries. Complex auroral structures, such as auroral streamers, poleward boundary intensifications (PBIs) and bifurcations (e.g., Forsyth et al., 2020; Henderson, 2012; Nishimura et al., 2011), can be observed near midnight during the expansion phase (b),(e) Same auroral images but overlaid with ionospheric (at 110 km altitude) footprints of ELFIN, THEMIS, and DMSP using T01 mapping in AACGM coordinates. The time stamps are indicated along the spacecraft trajectories with the cross symbols. (c and f) F18 (left) and F17 (right) measurements of plasma densities, magnetic field perturbations, and low-energy (<30 keV) electron and ion precipitation energy fluxes (in keV/cm^2-s-sr-eV).

can be well modeled. This supports our interpretation that the anisotropic wave-driven precipitation, observed by ELFIN near 01:32 UT in Figure 1d, is from the plasma sheet during the expansion phase. Note that there exists a ~20-min time separation between ELFIN-A and DMSP observations, and the DMSP image is time-aliased, being a composite of cross-track scans over the 12-min traversal of the southern polar region. Therefore, we do not examine the one-to-one correspondence between the DMSP-observed dynamic auroral features and ELFIN-A-observed energetic electron precipitation. We only identify the ELFIN-measured precipitation region relative to the DMSP large-scale auroral boundaries. Within the auroral oval, DMSP F17 SSJ5 measured interleaved Alfvénic and inverted-V auroral precipitations during the period of 01:57–02:10 UT (Karlsson et al., 2020; Liang et al., 2019).

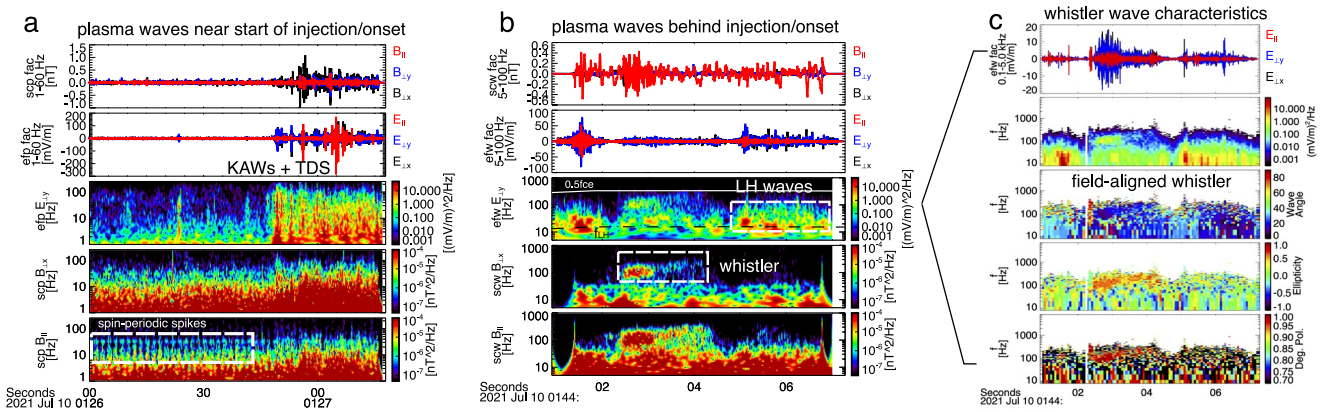

Figure 4. Magnetic and electric field waveforms and spectrograms measured from THEMIS-D particle-burst (512 samples per second (sps), DC-coupled) and wave-burst (16,384 sps, AC-coupled) collections, demonstrating various plasma waves associated with the plasma sheet electron injection. (a) Particle-burst data measured during the period of 01:26:00–01:27:20 UT, showing kinetic Alfvén waves and time domain structures. Panels from top to bottom are: low-frequency magnetic field waveforms, low-frequency electric field waveforms, wavelet spectrograms of $E_{\perp y}$, $B_{\perp x}$, and $B_{\parallel}$ in the field-aligned coordinates. The background magnetic field vector is determined by running a 1-min averaging window through spin-resolution magnetic fields (fgs data). Waveform data have been bandpass-filtered to be within 1–60 Hz. Spin-periodic contamination can be seen in both electric fields and magnetic fields. (b) Wave-burst collection during the period of 01:44:01–01:44:07, showing mostly lower-hybrid and whistler-mode waves. Panels are displayed in the same format as (a) but show waveforms with frequencies between 5 and 100 Hz and wave spectrograms up to 1 kHz. (c) Whistler-mode wave electric field waveform measurements and spectrograms of power spectral density, wave normal angle, wave ellipticity, and degree of polarization.

4. Plasma Waves Within Plasma Sheet Injection and Dipolarization Fields

Near the dipolarizing flux bundles (DFBs) at 01:27 UT, THEMIS observed intense broadband wave electric fields with frequencies up to 1 kHz and mean wave amplitudes of more than 10 mV/m below 60 Hz (Figure 1b). To reveal the nature of the broadband emissions, we show in Figure 4a the particle-burst waveform data (band-pass filtered within 1–60 Hz) measured at the beginning of the substorm injection within 01:26:00–01:27:20 UT. The waveform data demonstrate predominantly perpendicular fluctuations, in $B_{\perp x}$, $B_{\perp y}$, $E_{\perp x}$, and $E_{\perp y}$, with electric field perturbations up to 100 mV/m and magnetic field perturbations up to 1 nT. Their frequencies are much higher than the local ion cyclotron frequency of ∼0.5 Hz. These transverse field perturbations are consistent with the characteristics of KAWs (Chaston et al., 2012; Wygant et al., 2002). There are also large-amplitude nonlinear time domain structures (TDS) as evidenced by the spiky field-aligned E_z perturbations up to 300 mV/m near 01:27:05 UT (Mozer et al., 2015; Shen et al., 2021).

Short-duration (∼6 s) wave-burst data are available to show features of additional wave fluctuations collected at different time intervals during the substorm. These include whistler-mode waves, ECH waves, and lower-hybrid (LH) waves. These three modes are mainly observed after 01:40 UT when sustained electron injections have developed sufficient temperature anisotropy. In total, nine collections of ∼6-s wave-burst data were obtained in our event, with four of them showing mainly ECH waves near and above f_{ce} ∼600 Hz that were also accompanied by low-frequency broadband waves below ∼100 Hz. The broadband waves consisted mainly of either KAWs or LH waves. LH waves have frequencies near and above the lower-hybrid frequency (∼20 Hz) and can be distinguished from KAWs by examining whether B_z dominates magnetic fluctuations (Graham et al., 2017). Figure 4b demonstrates an example of these LH wave bursts along with whistler-mode waves. The whistlers are in the frequency band of 0.1–0.35f_{ce} with peak wave spectral densities reaching up to 10^{-4} nT^2/Hz. A detailed analysis of the whistler-mode wave spectra has been provided in Supporting Information S1. In Figure 4c, we analyze the whistler-mode wave normal angle, ellipticity, and degree of polarization using Means' method (Means, 1972). These whistler-mode waves mainly propagate along the magnetic field ($|\theta_{kb}| < 25°$), which is typical in the equatorial plasma sheet injection region (Breuillard et al., 2016; W. Li, Bortnik, et al., 2011; Le Contel et al., 2009; X. Zhang et al., 2018).

5. Potential Waves Generating Energetic Electron Pitch-Angle Diffusion and Precipitation

We now embark on the main question we aim to address in this paper: To what plasma waves or electron scattering mechanisms can we attribute the anisotropic, energetic (approximately 50–300 keV) electron precipitation

observed by ELFIN-A near 01:32 UT in Figure 1d? On the one hand, the anisotropic precipitation has higher loss cone filling rates at lower energies, thus disproving field-line curvature (FLC) scattering as a viable mechanism. On the other hand, we have observed various wave modes in the equatorial plasma sheet during the substorm, among which ECH waves and TDSs have been known to mainly scatter electrons with energies below a few keV (Ni et al., 2016; Shen et al., 2021; Vasko et al., 2017, 2018). LH waves and magnetosonic waves cannot scatter energetic electrons effectively into the loss cone (e.g., Ma et al., 2016; Mourenas et al., 2013). In addition, MHD ULF waves associated with injections (Runov et al., 2014; Shiokawa et al., 1997) are unlikely to directly impact energetic electrons in pitch angle (e.g., Lejosne & Kollmann, 2020; Ukhorskiy & Sitnov, 2013, and references therein). Instead, ULF waves may contribute indirectly to electron pitch-angle scattering by coupling with and seeding the growth of other kinetic-scale waves (X. J. Zhang et al., 2020), such as KAWs (Allan & Wright, 2000; Hasegawa & Chen, 1975) or whistler-mode waves (L. Li et al., 2022; W. Li, Thorne, et al., 2011; Xia et al., 2016; X.-J. Zhang et al., 2019). Note that electromagnetic ion cyclotron (EMIC) waves, which can also scatter energetic electrons, were absent in this event and, regardless, they typically contribute to relativistic (>500 keV) electron precipitation, that is, energies well above those of interest in this study. The electron resonant energies are in fact higher as the plasma density gets lower (i.e., magnetic energy per particle increases), as is the case in the plasma sheet (Albert, 2003; Angelopoulos et al., 2022; Mourenas et al., 2016; Ni et al., 2015; Summers & Thorne, 2003). We are, therefore, left with two wave modes—whistler-mode waves and KAWs—to potentially explain the anisotropic electron precipitation observed by ELFIN-A during the substorm expansion phase.

Previous studies have shown that the scattering efficiency of plasma sheet electrons by parallel whistler-mode waves drops significantly at energies increasing from 10 keV to 50–100 keV (Artemyev et al., 2022; Ghaffari et al., 2021; Ni, Thorne, Meredith, et al., 2011; Ni, Thorne, Shprits, et al., 2011; Panov et al., 2013). The corresponding electron minimum resonant energy is ∼5 keV in our case. To estimate energetic electron diffusion rates driven by the observed parallel-propagating whistlers, we have employed the formula of whistler-driven electron local diffusion rates derived by Summers (2005), which only accounts for the first-order cyclotron resonant interaction. However, this solution has been found to be a reasonable approximation for mildly oblique (<25°) whistler-mode waves, albeit resulting in a slight overestimate of the scattering rates (Albert, 2007; Shprits et al., 2006; Summers et al., 2007). Electron local diffusion coefficients we calculated for whistler-mode waves are also validated via benchmarking with the example shown in Figure 1 of Summers (2005). Although rare in the nightside plasma sheet (e.g., W. Li, Bortnik, et al., 2011), in case whistler-mode waves have highly oblique wave normal angles, higher-order resonances need to be considered. Several other studies have provided analytical formulae of calculating electron diffusion rates due to oblique whistler-mode waves (e.g., Albert, 2017; Artemyev et al., 2013, 2016; Mourenas et al., 2012).

Bounce averaging takes into account the latitudinal distribution of waves and the interaction time between the waves and electrons as electrons travel along the magnetic field line between mirror points. We approximate this procedure by weighting the local diffusion rates with fractional wave-particle interaction time relative to the bounce period τ_w/τ_b, where τ_w is the time the electron spend within the wave region and τ_b is the bounce period. The weighting factors are calculated for electrons with different equatorial pitch angles in the plasma sheet dipolarized magnetic field. We adopt this approximate procedure because: (a) statistical studies have shown that parallel whistler-mode waves are mainly confined to equatorial regions in the plasma sheet at nightside (Agapitov et al., 2018; W. Li, Bortnik, et al., 2011; Meredith et al., 2021), thus there is little contribution from off-equator whistlers; and (b) it is very challenging to analytically incorporate a model field that is accurate enough to describe the dipolarized plasma sheet and current sheet into the procedure of evaluating bounce-averaged diffusion coefficients (e.g., Ni, Thorne, Shprits, et al., 2011).

Using the approximate procedure outlined above, we have obtained whistler-driven bounce-averaged diffusion coefficients $D_{\alpha_0\alpha_0}$ on the order of 10^{-2} s^{-1} for near-loss-cone electrons with pitch angles $\alpha < 10°$ at 10 keV. The diffusion rates decrease drastically to about 10^{-7}–10^{-6} s^{-1} at 50–100 keV and about 10^{-8} s^{-1} at 200 keV and higher energies. Accounting for a scaling factor of ΔB^2, these $D_{\alpha_0\alpha_0}$ are roughly consistent, in terms of order of magnitude, with previous studies at low energies (tens of keV) (Ni et al., 2012; Ni, Thorne, Shprits, et al., 2011). The whistler-mode wave amplitude in our case is a strong emission example ($\Delta B \simeq 220$ pT), compared with very weak amplitudes (up to tens of pT) of whistler-mode waves as reported from statistical observations at $L > 8$ at nightside (W. Li, Bortnik, et al., 2011). We have provided a detailed analysis of the whistler-mode waves observed in Figure 4b and the procedure of calculating whistler-driven bounce-averaged diffusion coefficients in Supporting Information S1.

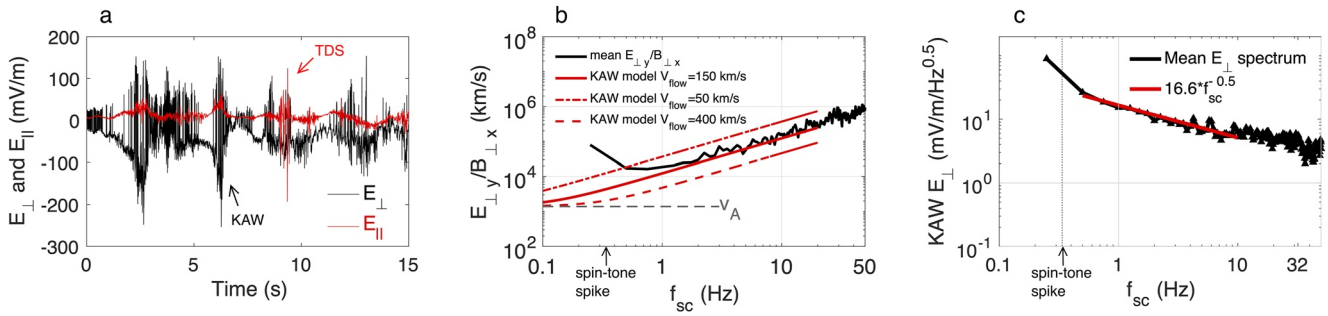

Figure 5. (a) Particle-burst waveform data showing kinetic Alfvén wave (KAW) perpendicular and parallel electric fields during the 15-s interval of 01:26:46–01:27:01 UT. The perpendicular electric fields are calculated as $E_{\perp} = \mathrm{sgn}(E_{\perp y})\sqrt{E_{\perp x}^2 + E_{\perp y}^2}$, where sgn is the sign function. (b) Mean $E_{\perp y}/B_{\perp x}$ spectra (black) calculated for the same period in panel (a) in comparison with the model prediction of KAW dispersion relation, using the THEMIS-observed range of ion flow velocities (50, 150, and 400 km/s in red lines). The plasma parameters used for the KAW model are based on THEMIS observations at this time, which have been provided in Supporting Information S1. We exclude from the calculation the background spectra of those with $E_{\perp y}$ amplitudes less than 10 mV/m and $B_{\perp x}$ amplitudes less than 0.1 nT at 0.25 Hz. The spectra are calculated using Hanning windows of 4 s with 2-s overlapping. The local Alfvén speed v_A ~1,400 km/s is shown as the gray dashed line. Note that the spurious spectral amplitude increase near 0.33 Hz is due to spin-periodic spikes in the DC-coupled electric field measurements (Bonnell et al., 2008). (c) Least-square power-law fitting of the mean KAW $E_{\perp}$ spectra for the same interval in (a).

To analyze energetic electron scattering by KAWs, we further explore the spectral characteristics of KAWs measured near 01:27 UT in Figure 4a. These in-situ wave measurements provide important observables to inform our analyses and simulations on the interactions between KAWs and electrons. Figure 5a displays an exploded view of the parallel and perpendicular electric fields of KAWs measured during the 15-s period of 01:26:46–01:27:01 UT, in the beginning of the substorm injection. The perpendicular electric fields have small-scale fluctuations embedded within the large-scale fields that reach more than 200 mV/m. We also observe transient $E_{\parallel}$ spikes of time domain structures (TDSs) during the interval.

We use the same procedure as reported by Shen et al. (2022c) to identify KAWs, that is, by comparing the measured $E_{\perp y}/B_{\perp x}$ spectra (in the field-aligned coordinates) with the theoretical KAW dispersion relation. The spacecraft-frame frequencies of broadband KAWs well exceed the local ion cyclotron frequency and thus have been interpreted to be in great part due to the Doppler shift of low-frequency KAW structures overtaken by a local ion flow (Chaston et al., 2012; Stasiewicz et al., 2000):

$$\left|\frac{E_{\perp y}}{B_{\perp x}}\right| = v_A\left(1 + k_{\perp}^2\rho_i^2\right)\left[1 + k_{\perp}^2\left(\rho_i^2 + \rho_s^2\right)\right]^{-1/2}, \quad (1)$$

where based on THEMIS-D observations of a background magnetic field $B_0 \simeq 35$ nT, an average ion number density $n_i \simeq 0.3$ cm^{-3}, $T_e \simeq 2.5$ keV, $T_i \simeq 3.5$ keV, the local Alfvén speed is $v_A = B_0/\sqrt{\mu m_i n_i}$ ≃1,400 km/s, $k_{\perp} \simeq 2\pi f_{sc}/v_i$ is the KAW perpendicular wavenumber inferred from the spacecraft frame frequency f_{sc} and perpendicular ion flows v_i in the range of 50–~500 km/s, and ρ_i, ρ_s are the ion thermal gyroradius and ion acoustic gyroradius. These plasma and field parameters are based on observations in Figure 1b, the details of which have also been provided in Supporting Information S1. Figure 5b demonstrates that the measured mean wave fields (the black curve) are consistent with those predicted by the KAW model (the red lines), for an average ion flow velocity of 150 km/s, similar to that measured by THEMIS-D (Figure 1b). The measured spectra are consistent with KAWs in frequencies from ~0.5 Hz to more than 20 Hz, corresponding to $k_{\perp}\rho_i$ ~5–200 in the kinetic branch (Lysak & Lotko, 1996). Figure 5c presents the fitted power-law spectrum of the mean $E_{\perp}$ field as $E_f = E_0 f_{sc}^{-\nu}$ (mV/m/$\sqrt{Hz}$), where $E_0 = 16.6$ mV/m and $\nu = 0.5$. The KAW electric field amplitudes and the spectral power-law index obtained in our substorm event are large but within family when compared with previous statistical observations of the average power of KAWs in the plasma sheet (Chaston et al., 2012; Ergun et al., 2020) and injection region (Chaston et al., 2015, 2018).

Next, we evaluate electron bounce-averaged diffusion coefficients driven by the observed KAWs using test particle simulations (Shen et al., 2022c). We apply a generalized guiding-center model (Cary & Brizard, 2009; Ukhorskiy et al., 2011) including electron bounce motion in a magnetic field that models the Earth's plasma sheet

with an embedded dipolarization front. The equations of motion are derived as (Cary & Brizard, 2009; Ukhorskiy et al., 2011):

$$\frac{d\mathbf{R}}{dt} = \frac{p_{\parallel}}{m_e\gamma}\frac{\mathbf{B}^*}{B_{\parallel}^*} + \mathbf{E}^* \times \frac{c\mathbf{b}}{B_{\parallel}^*}, \quad \frac{dp_{\parallel}}{dt} = \frac{q_e\mathbf{E}^* \cdot \mathbf{B}^*}{B_{\parallel}^*} \tag{2}$$

where $\mathbf{R}$ is the guiding center position, $p_{\parallel}$ is the electron parallel momentum, $\mathbf{b}$ is the magnetic unit vector, q_e is the electron charge, and $\mathbf{E}^*$ and $\mathbf{B}^*$ are the effective electric field (mainly dictated by waves) and magnetic field. We use the following magnetic field to model the Earth's large-scale plasma sheet, current sheet, and dipolarization front fields in the Geocentric Solar Magnetospheric (GSM) coordinates:

$$\begin{aligned}\mathbf{B}_0 = {} & B_{CS}\,tanh\left(\frac{z}{L_{CS}}\right)\mathbf{e}_x + aB_{CS}\mathbf{e}_z \\ & + B_{CS}\left(a\sin^{-2}\alpha_{LC} - 1\right)\tanh\left(\frac{z}{L_{PS}}\right)\mathbf{e}_x \\ & + B_{DF}\left[1 - \tanh\left(\frac{x - v_{DF}t}{L_{DF}}\right)\right]\mathbf{e}_z\end{aligned} \tag{3}$$

where the first term describes the current sheet field with z-gradients having a scale length of L_{CS} and a magnitude of B_{CS}. The third term describes the large-scale magnetic field z-gradients with a scale length L_{PS} and a magnitude of B_{CS}, to allow electron bounce motion along the field line. The last term describes the dipolarization front field with x-gradients having a scale length of L_{DF} and a magnitude B_{DF}. Parameter a determines the level of magnetic field line stretching in the pre-dipolarized current sheet (i.e., the ratio of magnitudes of the magnetic field components in z and x directions). The term $\sim(a\sin^{-2}\alpha_{LC} - 1)$ mimics the magnetic field increase on the earthward side to maintain a realistic loss-cone size for the current sheet model. A more detailed description of the simulation and a discussion of the assumptions and limitations of the model can be found in Shen et al. (2022a).

Taking into account electron bounce motion and perpendicular guiding-center drifts within the dipolarization front, Shen et al. (2022a) have shown that electrons with energies of tens to hundreds of keV can be pitch-angle scattered into the loss cone by KAWs, through Doppler-shifted Landau resonance near the magnetic equator. The resonance condition can be approximated as $v_{\parallel} \simeq -k_{\perp}v_{drift}/k_{\parallel} = -v_{drift}\tan\theta$, where $v_{\parallel}$ is the resonant electron parallel velocity, v_{drift} is the curvature and gradient drift of the electron, and θ is the KAW wave normal angle, which is typically larger than 70°(Chaston et al., 2009).

To estimate KAW-driven diffusion rates for near-loss-cone electrons (i.e., $\alpha = 1.5°$, see X.-J. Zhang et al., 2015) in our event, we have specified broadband electrostatic KAW potentials having 39 harmonics $k_{\perp}$ increasing with a stepsize of $\Delta k_{\perp}\rho_i \sim 1.3$ in the range of $k_{\perp}\rho_i \in [3, 51]$. This range corresponds to the spacecraft frame frequency range of [0.25,5] Hz, taking into account an ion plasma flow $v_i \sim 150$ km/s. KAWs have been frequently observed both at the equator and near the plasma sheet boundary layer (Angelopoulos et al., 2002; Chaston et al., 2012; Wygant et al., 2002), but their propagation toward higher latitudes (away from the equator) is suppressed by damping due to their Landau-resonance with suprathermal electrons (e.g., Gurram et al., 2021; Sharma Pyakurel et al., 2018). The wave distribution is assumed to be limited within $z \in [-2L_{CS}, 2L_{CS}]$ and $x \in [-2L_{DF}, 2L_{DF}]$ centered around the equatorial current sheet and dipolarization front region. To obtain the characteristic KAW wave amplitude E_{θ}, which dictates the fractional wave power at individual wave normal angles that are optimum to scatter resonant electrons at different energies, we assume an isotropic wave normal angle distribution $F(\theta)$ within [83°, 87°]. This angle range accounts for optimal resonance energies of ~50–300 keV in the model. Accordingly, we have $F(\theta) = 1/4$ for $d\theta \sim 1°$ and E_{θ} is determined as $E_{\theta} = \sqrt{\left(\sqrt{\sum E_f^2 df}\right)^2 F(\theta)d\theta} = 6$ mV/m, where the spectrum E_f has been obtained from Figure 5c. The KAW spectrum in the simulation is then $E_{\perp} = E_{\theta}(f_{sc}/2\pi)^{-\nu}$ and $\nu \sim 0.5$. The parallel electric fields are included based on the KAW polarization relation. The large-scale background magnetic field parameters here are same as those in Shen et al. (2022a).

Figure 6 displays KAW-driven electron bounce-averaged diffusion coefficients $D_{\alpha_0\alpha_0}$ as a function of energy, evaluated at an equatorial pitch angle of 1.5°. To explore variations in $D_{\alpha_0\alpha_0}$ due to variations in magnitude of the dipolarization front B_{DF}, we perform two sets of simulations using $B_{DF} = 10$ nT (the purple solid curve) and $B_{DF} = 20$ nT (the black solid curve), according to the observed value range in Figure 1b. The decrease of B_{DF} from 20 to 10 nT leads to an increase of $D_{\alpha_0\alpha_0}$ by a factor of ~3 above 50 keV. Note, however, that as B_{DF}

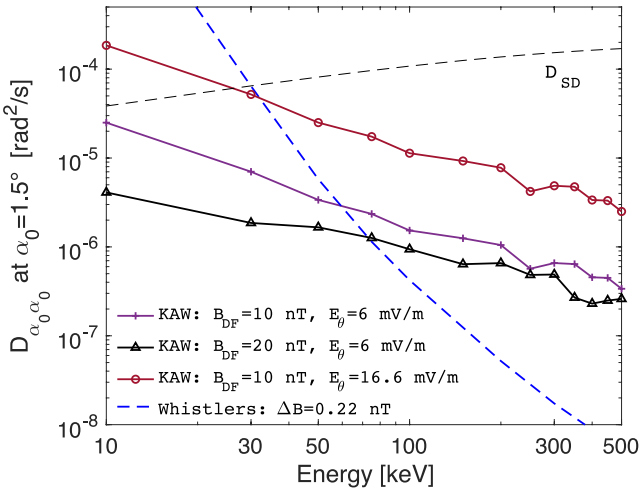

Figure 6. Electron bounce-averaged diffusion coefficients $D_{\alpha_0\alpha_0}$ as a function of energy for an equatorial pitch angle $\alpha_0 = 1.5°$ due to resonant scattering by the observed kinetic Alfvén waves (KAWs) (solid lines) and whistler-mode (blue dashed line) waves from THEMIS. The simulation background field parameters for KAW-electron scattering are: $B_{CS} = 20$ nT, $L_{CS} = 3{,}000$ km, $B_{DF} = 20$ nT (black solid line) or 10 nT (purple solid line), $L_{DF} = 500$ km, which is about three times the local ion gyroradius of ~145 km, $L_{PS} = 5\ R_E$, $\alpha_{LC} = \arcsin\left(\sqrt{B_{eq}/B_{iono|100km}}\right) = 1.5°$ in our event. The KAW broadband spectrum has $E_\theta = 6$ mV/m, $\nu = 0.5$, where the KAW wave normal angle θ is assumed uniform within [83°, 87°] (see the text and additional details in Shen et al. (2022a)). To account for full ranges of KAW power in observations, we also show $D_{\alpha_0\alpha_0}$ with KAW $E_\theta = 16.6$ mV/m (red solid line) as observed in Figure 5c. The KAW-driven diffusion coefficients are obtained by ensemble-averaging the pitch-angle variance of electrons after one bounce period. The electron bounce-averaged $D_{\alpha_0\alpha_0}$ driven by the observed whistler waves are shown as the blue dashed line. The black dashed line shows the strong diffusion limit $D_{SD} = (\alpha_{LC})^2/2\tau_b \sim 10^{-4}\ s^{-1}$, where $\alpha_{LC} \sim 1.5°$ (see Kennel and Petschek (1966) for D_{SD} definition).

decreases further, the field-line curvature radius of the magnetic field will become small enough to initiate non-adiabatic curvature/current-sheet scattering, which is undesirable as its effects have not been included in our simulation. For $B_{DF} = 10$ nT, the obtained KAW-driven $D_{\alpha_0\alpha_0}$ approach the strong diffusion limit D_{SD} (Kennel & Petschek, 1966) at 10 keV, and decrease gradually to the order of 10^{-5}–$10^{-6}\ s^{-1}$ for ~30–300 keV. In addition, to account for a possible range of KAW wave power as observed in Figure 5c, we show $D_{\alpha_0\alpha_0}$ under the KAW characteristic amplitude $E_\theta = 16.6$ mV/m (the solid red line). This larger wave power increases $D_{\alpha_0\alpha_0}$ by nearly an order of magnitude, with ≤~30 keV electrons exceeding the strong diffusion limit. In comparison, we have also shown whistler-driven electron diffusion rates (the blue dashed line), which are much smaller than those driven by KAWs at energies above 50 keV in this event. However, the observed parallel whistler-mode waves may have a stronger scattering effect for electrons below ~50 keV in the plasma sheet.

It is worth emphasizing that in the quasi-linear regime the simulated KAW-driven electron diffusion coefficients scale with E_θ^2 (e.g., Kennel & Engelmann, 1966; Shapiro & Sagdeev, 1997), which largely hinges on KAW wave normal distributions. Although we cannot obtain the KAW wave normal angle distribution in our case and no statistical KAW normal measurements have thus far emerged (to the best of our knowledge), we can understand this effect by varying the assumed θ distributions. For instance, if we assume KAWs are uniformly distributed within [80°, 89°] as opposed to within [83°, 87°], this results in E_θ ~3.8 mV/m compared with 6 mV/m used in Figure 6, leading to a decrease in $D_{\alpha_0\alpha_0}$ by a factor of 2.5.

To compare with the loss cone filling ratios observed by ELFIN in Figure 1d, we can tentatively assume a steady-state diffusion equilibrium to relate the precipitating differential fluxes within the loss cone ($0 < \alpha_{eq} \le \alpha_{LC}$, where $\alpha_{LC} = 1.5°$) to those at the loss cone angle as (Kennel & Petschek, 1966; W. Li et al., 2013; Reidy et al., 2021; Mourenas et al., 2021; Shen et al., 2022b):

$$J_{eq}(E, \alpha_{eq}) = J_{eq}(E, \alpha_{LC}) \cdot \frac{I_0\left(\frac{\alpha_{eq}}{\alpha_{LC}} Z_0\right)}{I_0(Z_0)} \tag{4}$$

and the precipitating differential fluxes outside but near the loss cone ($\alpha_{LC} \le \alpha_{eq}$) to those at the loss cone as:

$$J_{eq}(E, \alpha_{eq}) = J_{eq}(E, \alpha_{LC}) \cdot \left[1 + \ln\left(\frac{\sin\alpha_{eq}}{\sin\alpha_{LC}}\right)\frac{Z_0 I_1(Z_0)}{I_0(Z_0)}\right] \tag{5}$$

where $Z_0 \simeq \alpha_0/\sqrt{D_{\alpha_0\alpha_0|LC}\tau}$ is an energy-dependent parameter defining the diffusion strength at the loss cone, τ is assumed to be a quarter of the bounce period, I_0 and I_1 is the modified Bessel function. Assuming adiabatic motion of energetic electrons along the field line, the precipitating-to-perpendicular flux ratios measured by ELFIN can be approximated as (e.g., Mourenas et al., 2021; Shen et al., 2022b):

$$\frac{J_{preci|50°}}{J_{trapped|80°}} \simeq \frac{\int_0^{2\pi}\int_0^{\beta} J_{eq}(E, \alpha_{LC})\frac{I_0\left(\frac{\alpha_{eq}}{\alpha_{LC}} Z_0\right)}{I_0(Z_0)}\sin\eta d\eta d\psi}{\int_0^{2\pi}\int_0^{\beta} J_{eq}(E, \alpha_{LC}) \cdot \left[1 + \ln\left(\frac{\sin\alpha_{eq}}{\sin\alpha_{LC}}\right)\frac{Z_0 I_1(Z_0)}{I_0(Z_0)}\right]\sin\eta d\eta d\psi}, \tag{6}$$

where β is the detector half angle ~11.25°, η and ψ are related to the precise local pitch angle α of electrons within an elementary solid angle surface area as seen by the ELFIN detector, and the term $J_{eq}(E, \alpha_{LC})$ cancels for the ratio calculation. The averaged local pitch angles for precipitating and trapped fluxes measured by ELFIN are ~50° and ~80° in the above calculation. Given $D_{\alpha_0\alpha_0|LC} \simeq D_{\alpha_0\alpha_0|1.5°}$ as shown in Figure 6, we have obtained precipitating-to-perpendicular flux ratios for 50–150 keV electrons in the range of ~0.01–~0.08 with

$E_\theta = 6$ mV/m. To account for variations in KAW normal distribution and wave power, we also calculate the ratios corresponding to $E_\theta = 16.6$ mV/m (an upper limit of the wave power), which is in the range of ~0.1–~0.4. These values are comparable but slightly lower than the observed ratios, which are mostly in the range of ~0.1–~0.6 in Figure 1d.

To understand this difference, we note that the above calculation is valid only for steady-state diffusion equilibrium when the injection source at high pitch angles ($\alpha \sim 90°$) is completely balanced by the precipitation into the loss cone (Kennel & Petschek, 1966). In reality, however, the diffusion hardly reaches equilibrium on the time scales of substorm expansion. It is anticipated that the distribution within the loss cone may still be controlled by the balance of loss and wave scattering with a rate $D_{\alpha\alpha}$ under the weak diffusion limit, thus the solution inside the loss cone is again close to an exponential function determined as $f(\alpha_{in}) \sim I_0\left(\alpha/\sqrt{D_{\alpha\alpha}\tau}\right)$. This implies that the numerator in Equation 6 may still be valid. However, the solution exterior to the loss cone under the non-equilibrium condition is mainly determined by the instantaneous pitch-angle distribution, which in our case takes the form $f(\alpha_{out}) \sim \sin^n \alpha$ where $n \simeq 0.2$ (see Figure S3 in Supporting Information S1).

Consider again the steady-state solution outside the loss cone, which is a logarithmic function $f(\alpha_{out}) = (S^*/D_{\alpha\alpha})\ln(\sin\alpha) + f_c$, where f_c is a constant determined by matching the outside solution to that inside the loss cone at $\alpha = \alpha_{LC}$ (Kennel & Petschek, 1966). The full steady-state solution is $f(\alpha_{out}) = (S^*/D_{\alpha\alpha})\left\{h(\alpha_{LC}) + \ln\left(\frac{\sin\alpha}{\sin\alpha_{LC}}\right)\right\}$, where the term $h(\alpha_{LC}) = I_0(Z_0)/Z_0 I_1(Z_0)$ is evaluated from the functional form within the loss cone, and the term $\ln\left(\frac{\sin\alpha}{\sin\alpha_{LC}}\right)$ is determined by the functional form outside the loss cone and contributes primarily to the flux outside the loss cone. Note that $(S^*/D_{\alpha\alpha})\ln\left(\frac{\sin\alpha}{\sin\alpha_{LC}}\right)$ can also be written as $f(\alpha_{out}) - f(\alpha_{LC}) = f'(\alpha_{LC})d\alpha \sim d\alpha/\alpha$. Consider now the non-equilibrium diffusion during the expansion phase with the observed distribution outside the loss cone $f(\alpha_{out}) \sim \sin^n\alpha$. Then, $f(\alpha_{out}) - f(\alpha_{LC}) = f'(\alpha_{LC})d\alpha \sim d\alpha/\alpha \cdot n\sin^n\alpha < d\alpha/\alpha$. Therefore, the corresponding denominator in Equation 6 will be smaller, and the precipitating-to-perpendicular flux ratio will be larger during the expansion phase than during the steady-state equilibrium. Therefore, the anisotropic energetic electron precipitation from the plasma sheet observed by ELFIN-A near 01:32 UT in Figure 1d is likely consistent with pitch-angle scattering by the observed KAWs during the substorm expansion phase.

To summarize this section, we have combined in-situ wave measurements, theoretical quasi-linear estimates, and numerical test particle simulations to investigate the relative role of the observed KAWs and whistler-mode waves at THEMIS, in driving the scattering and precipitation of energetic electrons from the plasma sheet during our substorm event. We first outline the procedures of estimating whistler-driven electron bounce-averaged diffusion rates and then analyze the wave spectral characteristics of KAWs which inform our numerical test particle simulations on KAW-electron interactions. These are followed by a brief description of the numerical model that we employ to estimate KAW-driven bounce-averaged electron pitch-angle diffusion rates. Finally, we show that KAW-driven electron diffusion rates are comparatively much smaller than those driven by the observed whistler-mode waves at energies above 50 keV. Also, based on quasi-linear diffusion analyses, we have deduced that the diffusion rates due to KAWs are roughly consistent with the precipitating-to-perpendicular anisotropy flux ratios measured by ELFIN-A. Thus, the KAWs dominate over whistler-mode waves in driving the anisotropic, energetic electron precipitation observed by ELFIN-A near 01:32 UT in Figure 1d.

6. Discussion and Conclusion

Using approximately conjugate observations made from a fleet of spacecraft including the THEMIS, ELFIN, and DMSP missions, we have analyzed comprehensive measurements of the energetic electron precipitation, the magnetospheric injection, and the associated plasma waves to examine the role of plasma waves in scattering injected electrons into the loss cone in the plasma sheet during a substorm. While ELFIN-B observed primarily weak isotropic electron precipitation in the ionosphere, with energies of 50–200 keV, driven by magnetospheric field-line curvature scattering during the growth phase, ELFIN-A observed intensified anisotropic electron precipitation at energies extending to >300 keV during the expansion phase. This anisotropic precipitation is likely driven by wave-particle interactions, as inferred by the loss cone filling ratios (the precipitating-to-perpendicular flux ratios) of energetic electrons that have a characteristic energy dependence. An approximate demarcation between the plasma sheet and the radiation belt regions traversed by ELFIN is achieved by (a) the characteristic precipitation patterns of those regions, such as the IB, and by (a) DMSP FUV auroral images, which provide

observations of the auroral boundaries during the substorm event. At the equatorial plasma sheet, THEMIS-D observed prolonged energetic electron injections in the nightside transition region ($R \sim 11\ R_E$, $MLT \sim 0$ hr), along with intense KAWs that are associated with ELFIN energetic electron precipitation. Field-aligned propagating whistler-mode waves, along with several other wave modes, have also been observed by THEMIS-D, primarily ∼10-min after the ELFIN observation of energetic electron precipitation. The observed injection electron flux energy distributions, by THEMIS-D in the plasma sheet, are also in good agreement with those measured by ELFIN within the ionospheric wave-driven precipitation region. This agreement in distribution strongly supports our interpretation that ionospheric and magnetospheric observations are approximately conjugate.

We then used numerical test particle simulations with a dipolarized plasma sheet model to quantify electron pitch-angle diffusion coefficients driven by KAWs (Shen et al., 2022a) as measured from THEMIS. Electron bounce motion has been included in the model in order to quantify bounce-averaged electron diffusion rates. The resulting KAW-driven diffusion coefficients $D_{\alpha_0\alpha_0}$ for 50–500 keV near-loss-cone electrons are on the order of 10^{-6}–10^{-5} rad^2/s, compared with the strong diffusion limit $D_{\mathrm{SD}} \sim 10^{-4}$ rad^2/s at this radial distance ($\sim 11 R_E$) (Kennel & Petschek, 1966). Based on quasilinear theory, these KAW-driven diffusion rates predict energetic electron loss cone filling ratios roughly consistent with ELFIN observations in the ionosphere. On the other hand, the estimated $D_{\alpha_0\alpha_0}$ due to parallel whistler-mode waves are on the order of 10^{-8}–10^{-6} rad^2/s for 50–500 keV electrons. These are more than one order of magnitude smaller than those due to KAWs. In addition, whistler-mode waves were observed by THEMIS-D ∼10 min after ELFIN measurements of anisotropic electron precipitation from the plasma sheet. We conclude that the observed KAWs dominate over the observed whistler-mode waves in the scattering and precipitation of energetic (∼50–∼300 keV) electrons from the dipolarized plasma sheet during our event. Such wave-driven precipitation has been directly observed and well-resolved in pitch angle by ELFIN during the substorm injection.

Previous studies have shown that ion bursty bulk flows, flow shear, and magnetic compression facilitate the generation of high-power MHD Alfvén waves in the plasma sheet flow braking region (Angelopoulos et al., 2002; Chaston et al., 2012; Kepko et al., 2014; Shiokawa et al., 1997). Through mode-coupling (Hasegawa & Chen, 1975; Johnson & Cheng, 2001; Lin et al., 2012), phase-mixing (Allan & Wright, 2000), or other nonlinear processes (e.g., Wygant et al., 2002), the large-scale MHD waves can effectively couple and transfer significant energy to KAWs at or near plasma boundaries, such as dipolarization fronts and injection boundaries (Deng et al., 2010; Ergun et al., 2015; Malaspina et al., 2015; Usanova & Ergun, 2022). These KAWs can accelerate and heat thermal electrons (Artemyev et al., 2015; Damiano et al., 2015, 2016; Watt & Rankin, 2009) and ions (Chaston et al., 2013, 2014; Johnson & Cheng, 2001) and seed the growth of electrostatic turbulence down to electron scales (An et al., 2021). Such kinetic processes facilitate multi-scale energy coupling and dissipation associated with plasma injections, magnetic field dipolarizations, and fast ion jets in the substorm plasma sheet. To complement this picture, the results of our paper have provided convincing evidence that KAWs can also contribute to and may even dominate energetic injection electron scattering and precipitation processes in the dipolarized plasma sheet during substorm events. It requires future investigations to fully understand how significant this KAW-driven energetic precipitation is on the global scale, at different times, and in a statistical sense.

Data Availability Statement

ELFIN data can be publicly accessed from https://data.elfin.ucla.edu/. DMSP data products can be accessed from https://www.ncei.noaa.gov/data/dmsp-space-weather-sensors/access/, http://sd-www.jhuapl.edu/Aurora/, and https://ssusi.jhuapl.edu/data_products. THEMIS data is avaliable at http://themis.ssl.berkeley.edu. SuperMAG SML data can be obtained from https://supermag.jhuapl.edu/indices/. Data access and processing was done using SPEDAS V4.1, see Angelopoulos et al. (2019).

Acknowledgments
This work has been supported by NASA projects 80NSSC22K0517, 80NSSC21K0729, 80NSSC23K0108, 80NSSC20K1325, 80NSSC22K1005, and NAS5-02099. We also acknowledge NSF support under grant AGS-2019950. We are grateful to NASA's CubeSat Launch Initiative for ELFIN's successful launch in the desired orbits. We acknowledge critical contributions of numerous ELFIN undergraduate student interns and volunteers. We thank Johns Hopkins University Applied Physics Laboratory for providing the DMSP/SSUSI auroral FUV data and DMSP/SSJ data. We gratefully acknowledge the SuperMAG collaborators (https://supermag.jhuapl.edu/info/?page=acknowledgement).

References

Agapitov, O. V., Mourenas, D., Artemyev, A. V., Mozer, F. S., Hospodarsky, G., Bonnell, J., & Krasnoselskikh, V. (2018). Synthetic empirical chorus wave model from combined Van Allen Probes and cluster statistics. *Journal of Geophysical Research: Space Physics*, *123*(1), 297–314. https://doi.org/10.1002/2017JA024843

Akasofu, S.-I. (1964). The development of the auroral substorm. *Planatary Space Science*, *12*(4), 273–282. https://doi.org/10.1016/0032-0633(64)90151-5

Albert, J. M. (2003). Evaluation of quasi-linear diffusion coefficients for EMIC waves in a multispecies plasma. *Journal of Geophysical Research*, *108*(A6), 1249. https://doi.org/10.1029/2002JA009792

Albert, J. M. (2007). Simple approximations of quasi-linear diffusion coefficients. *Journal of Geophysical Research*, *112*(A12), 12202. https://doi.org/10.1029/2007JA012551

Albert, J. M. (2017). Quasi-linear diffusion coefficients for highly oblique whistler mode waves. *Journal of Geophysical Research*, *122*(5), 5339–5354. https://doi.org/10.1002/2017JA024124

Allan, W., & Wright, A. N. (2000). Magnetotail waveguide: Fast and Alfvén waves in the plasma sheet boundary layer and lobe. *Journal of Geophysical Research*, *105*(A1), 317–328. https://doi.org/10.1029/1999JA900425

An, X., Bortnik, J., & Zhang, X.-J. (2021). Nonlinear Landau resonant interaction between kinetic Alfvén waves and thermal electrons: Excitation of time domain structures. *Journal of Geophysical Research: Space Physics*, *126*(1), e28643. https://doi.org/10.1029/2020JA028643

Angelopoulos, V. (2008). The THEMIS mission. *Space Science Reviews*, *141*(1–4), 5–34. https://doi.org/10.1007/s11214-008-9336-1

Angelopoulos, V., Artemyev, A., Phan, T. D., & Miyashita, Y. (2020). Near-Earth magnetotail reconnection powers space storms. *Nature Physics*, *16*(3), 317–321. https://doi.org/10.1038/s41567-019-0749-4

Angelopoulos, V., Baumjohann, W., Kennel, C. F., Coronti, F. V., Kivelson, M. G., Pellat, R., et al. (1992). Bursty bulk flows in the inner central plasma sheet. *Journal of Geophysical Research*, *97*(A4), 4027–4039. https://doi.org/10.1029/91JA02701

Angelopoulos, V., Chapman, J. A., Mozer, F. S., Scudder, J. D., Russell, C. T., Tsuruda, K., et al. (2002). Plasma sheet electromagnetic power generation and its dissipation along auroral field lines. *Journal of Geophysical Research*, *107*(A8), 1181. https://doi.org/10.1029/2001JA900136

Angelopoulos, V., Cruce, P., Drozdov, A., Grimes, E. W., Hatzigeorgiu, N., King, D. A., et al. (2019). The Space Physics Environment Data Analysis System (SPEDAS). *Space Science Reviews*, *215*(1), 9. https://doi.org/10.1007/s11214-018-0576-4

Angelopoulos, V., McFadden, J. P., Larson, D., Carlson, C. W., Mende, S. B., Frey, H., et al. (2008). Tail reconnection triggering substorm onset. *Science*, *321*(5891), 931–935. https://doi.org/10.1126/science.1160495

Angelopoulos, V., Runov, A., Zhou, X. Z., Turner, D. L., Kiehas, S. A., Li, S. S., & Shinohara, I. (2013). Electromagnetic energy conversion at reconnection fronts. *Science*, *341*(6153), 1478–1482. https://doi.org/10.1126/science.1236992

Angelopoulos, V., Sibeck, D., Carlson, C. W., McFadden, J. P., Larson, D., Lin, R. P., et al. (2008). First results from the THEMIS mission. *Space Science Reviews*, *141*(1–4), 453–476. https://doi.org/10.1007/s11214-008-9378-4

Angelopoulos, V., Tsai, E., Bingley, L., Shaffer, C., Turner, D. L., Runov, A., et al. (2020). The ELFIN mission. *Space Science Reviews*, *216*(5), 103. https://doi.org/10.1007/s11214-020-00721-7

Angelopoulos, V., Zhang, X. J., Artemyev, A. V., Mourenas, D., Tsai, E., Wilkins, C., et al. (2022). Energetic electron precipitation driven by electromagnetic ion cyclotron waves from ELFIN's low altitude perspective. arXiv e-prints, arXiv:2211.15653.

Artemyev, A. V., Agapitov, O., Mourenas, D., Krasnoselskikh, V., Shastun, V., & Mozer, F. (2016). Oblique whistler-mode waves in the Earth's inner magnetosphere: Energy distribution, origins, and role in radiation belt dynamics. *Space Science Reviews*, *200*(1–4), 261–355. https://doi.org/10.1007/s11214-016-0252-5

Artemyev, A. V., Angelopoulos, V., Zhang, X.-J., Runov, A., Petrukovich, A., Nakamura, R., et al. (2022). Thinning of the magnetotail current sheet inferred from low-altitude observations of energetic electrons. *Journal of Geophysical Research: Space Physics*, *127*(10), e2022JA030705. https://doi.org/10.1029/2022JA030705

Artemyev, A. V., Mourenas, D., Agapitov, O. V., & Krasnoselskikh, V. V. (2013). Parametric validations of analytical lifetime estimates for radiation belt electron diffusion by whistler waves. *Annales Geophysicae*, *31*(4), 599–624. https://doi.org/10.5194/angeo-31-599-2013

Artemyev, A. V., Rankin, R., & Blanco, M. (2015). Electron trapping and acceleration by kinetic Alfven waves in the inner magnetosphere. *Journal of Geophysical Research*, *120*(12), 10305–10316. https://doi.org/10.1002/2015JA021781

Artemyev, A. V., Neishtadt, A. I., & Angelopoulos, V. (2022). On the role of whistler-mode waves in electron interaction with dipolarizing flux bundles. *Journal of Geophysical Research: Space Physics*, *127*(4), e30265. https://doi.org/10.1029/2022JA030265

Auster, H. U., Glassmeier, K. H., Magnes, W., Aydogar, O., Baumjohann, W., Constantinescu, D., et al. (2008). The THEMIS fluxgate magnetometer. *Space Science Reviews*, *141*(1–4), 235–264. https://doi.org/10.1007/s11214-008-9365-9

Baker, D. N., Stauning, P., Hones, E. W., Jr., Higbie, P. R., & Belian, R. D. (1981). Near-equatorial, high-resolution measurements of electron precipitation at l =6.6. *Journal of Geophysical Research*, *86*(A4), 2295–2313. https://doi.org/10.1029/JA086iA04p02295

Baumjohann, W., Paschmann, G., & Luehr, H. (1990). Characteristics of high-speed ion flows in the plasma sheet. *Journal of Geophysical Research*, *95*(A4), 3801–3809. https://doi.org/10.1029/JA095iA04p03801

Berkey, F. T., Driatskiy, V. M., Henriksen, K., Hultqvist, B., Jelly, D. H., Shchuka, T. I., et al. (1974). A synoptic investigation of particle precipitation dynamics for 60 substorms in IQSY (1964-1965) and IASY (1969). *Planatary Space Science*, *22*(2), 255–307. https://doi.org/10.1016/0032-0633(74)90028-2

Birn, J., Hesse, M., Nakamura, R., & Zaharia, S. (2013). Particle acceleration in dipolarization events. *Journal of Geophysical Research*, *118*(5), 1960–1971. https://doi.org/10.1002/jgra.50132

Birn, J., Runov, A., & Hesse, M. (2014). Energetic electrons in dipolarization events: Spatial properties and anisotropy. *Journal of Geophysical Research: Space Physics*, *119*(5), 3604–3616. https://doi.org/10.1002/2013JA019738

Birn, J., Thomsen, M. F., Borovsky, J. E., Reeves, G. D., McComas, D. J., Belian, R. D., & Hesse, M. (1998). Substorm electron injections: Geosynchronous observations and test particle simulations. *Journal of Geophysical Research*, *103*(A5), 9235–9248. https://doi.org/10.1029/97JA02635

Bonnell, J. W., Mozer, F. S., Delory, G. T., Hull, A. J., Ergun, R. E., Cully, C. M., et al. (2008). The electric field instrument (EFI) for THEMIS. *Space Science Reviews*, *141*(1–4), 303–341. https://doi.org/10.1007/s11214-008-9469-2

Breuillard, H., Le Contel, O., Retino, A., Chasapis, A., Chust, T., Mirioni, L., et al. (2016). Multispacecraft analysis of dipolarization fronts and associated whistler wave emissions using MMS data. *Geophysical Research Letters*, *43*(14), 7279–7286. https://doi.org/10.1002/2016GL069188

Buchner, J., & Zelenyi, L. M. (1989). Regular and chaotic charged particle motion in magnetotaillike field reversals: 1. Basic theory of trapped motion. *Journal of Geophysical Research*, *94*(A9), 11821–11842. https://doi.org/10.1029/JA094iA09p11821

Cairns, I. H., & McMillan, B. F. (2005). Electron acceleration by lower hybrid waves in magnetic reconnection regions. *Physics of Plasmas*, *12*(10), 102110. https://doi.org/10.1063/1.2080567

Cary, J. R., & Brizard, A. J. (2009). Hamiltonian theory of guiding-center motion. *Reviews of Modern Physics*, *81*(2), 693–738. https://doi.org/10.1103/RevModPhys.81.693

Chaston, C. C., Bonnell, J. W., Clausen, L., & Angelopoulos, V. (2012). Energy transport by kinetic-scale electromagnetic waves in fast plasma sheet flows. *Journal of Geophysical Research*, *117*(A9), 9202. https://doi.org/10.1029/2012JA017863

Chaston, C. C., Bonnell, J. W., Halford, A. J., Reeves, G. D., Baker, D. N., Kletzing, C. A., & Wygant, J. R. (2018). Pitch angle scattering and loss of radiation belt electrons in broadband electromagnetic waves. *Geophysical Research Letters*, *45*(18), 9344–9352. https://doi.org/10.1029/2018GL079527

Chaston, C. C., Bonnell, J. W., Kletzing, C. A., Hospodarsky, G. B., Wygant, J. R., & Smith, C. W. (2015). Broadband low-frequency electromagnetic waves in the inner magnetosphere. *Journal of Geophysical Research*, *120*(10), 8603–8615. https://doi.org/10.1002/2015JA021690

Chaston, C. C., Bonnell, J. W., & Salem, C. (2014). Heating of the plasma sheet by broadband electromagnetic waves. *Geophysical Research Letters*, *41*(23), 8185–8192. https://doi.org/10.1002/2014GL062116

Chaston, C. C., Johnson, J. R., Wilber, M., Acuna, M., Goldstein, M. L., & Reme, H. (2009). Kinetic Alfvén wave turbulence and transport through a reconnection diffusion region. *Physical Review Letters*, *102*(1), 015001. https://doi.org/10.1103/PhysRevLett.102.015001

Chaston, C. C., Yao, Y., Lin, N., Salem, C., & Ueno, G. (2013). Ion heating by broadband electromagnetic waves in the magnetosheath and across the magnetopause. *Journal of Geophysical Research*, *118*(9), 5579–5591. https://doi.org/10.1002/jgra.50506

Christon, S. P., Williams, D. J., Mitchell, D. G., Huang, C. Y., & Frank, L. A. (1991). Spectral characteristics of plasma sheet ion and electron populations during disturbed geomagnetic conditions. *Journal of Geophysical Research*, *96*(A1), 1–22. https://doi.org/10.1029/90JA01633

Clilverd, M. A., Rodger, C. J., Rae, I. J., Brundell, J. B., Thomson, N. R., Cobbett, N., et al. (2012). Combined themis and ground-based observations of a pair of substorm-associated electron precipitation events. *Journal of Geophysical Research*, *117*(A2). https://doi.org/10.1029/2011JA016933

Cully, C. M., Ergun, R. E., Stevens, K., Nammari, A., & Westfall, J. (2008). The THEMIS digital fields board. *Space Science Reviews*, *141*(1–4), 343–355. https://doi.org/10.1007/s11214-008-9417-1

Damiano, P. A., Johnson, J. R., & Chaston, C. C. (2015). Ion temperature effects on magnetotail Alfvén wave propagation and electron energization. *Journal of Geophysical Research*, *120*(7), 5623–5632. https://doi.org/10.1002/2015JA021074

Damiano, P. A., Johnson, J. R., & Chaston, C. C. (2016). Ion gyroradius effects on particle trapping in kinetic alfvn waves along auroral field lines. *Journal of Geophysical Research*, *121*(11), 10831–10844. https://doi.org/10.1002/2016JA022566

Delcourt, D. C., Martin, R. F., Jr., & Alem, F. (1994). A simple model of magnetic moment scattering in a field reversal. *Geophysical Research Letters*, *21*(14), 1543–1546. https://doi.org/10.1029/94GL01291

Deng, X., Ashour-Abdalla, M., Zhou, M., Walker, R., El-Alaoui, M., Angelopoulos, V., et al. (2010). Wave and particle characteristics of earthward electron injections associated with dipolarization fronts. *Journal of Geophysical Research*, *115*(A9), A09225. https://doi.org/10.1029/2009JA015107

Divin, A., Khotyaintsev, Y. V., Vaivads, A., André, M., Markidis, S., & Lapenta, G. (2015). Evolution of the lower hybrid drift instability at reconnection jet front. *Journal of Geophysical Research*, *120*(4), 2675–2690. https://doi.org/10.1002/2014JA020503

Drake, J. F., Swisdak, M., Cattell, C., Shay, M. A., Rogers, B. N., & Zeiler, A. (2003). Formation of electron holes and particle energization during magnetic reconnection. *Science*, *299*(5608), 873–877. https://doi.org/10.1126/science.1080333

Elphic, R. C., Thomsen, M. F., Borovsky, J. E., & McComas, D. J. (1999). Inner edge of the electron plasma sheet: Empirical models of boundary location. *Journal of Geophysical Research*, *104*(A10), 22679–22694. https://doi.org/10.1029/1999JA900213

Ergun, R. E., Ahmadi, N., Kromyda, L., Schwartz, S. J., Chasapis, A., Hoilijoki, S., et al. (2020). Particle Acceleration in strong turbulence in the Earth's magnetotail. *The Astrophysical Journal*, *898*(2), 153. https://doi.org/10.3847/1538-4357/ab9ab5

Ergun, R. E., Goodrich, K. A., Stawarz, J. E., Andersson, L., & Angelopoulos, V. (2015). Large-amplitude electric fields associated with bursty bulk flow braking in the Earth's plasma sheet. *Journal of Geophysical Research*, *120*(3), 1832–1844. https://doi.org/10.1002/2014JA020165

Ergun, R. E., Usanova, M. E., Turner, D. L., & Stawarz, J. E. (2022). Bursty bulk flow turbulence as a source of energetic particles to the outer radiation belt. *Geophysical Research Letters*, *49*(11), e98113. https://doi.org/10.1029/2022GL098113

Forsyth, C., Sergeev, V. A., Henderson, M. G., Nishimura, Y., & Gallardo-Lacourt, B. (2020). Physical processes of meso-scale, dynamic Auroral forms. *Space Science Reviews*, *216*(4), 46. https://doi.org/10.1007/s11214-020-00665-y

Fu, H. S., Khotyaintsev, Y. V., André, M., & Vaivads, A. (2011). Fermi and betatron acceleration of suprathermal electrons behind dipolarization fronts. *Geophysical Research Letters*, *381*(16), 16104. https://doi.org/10.1029/2011GL048528

Gabrielse, C., Angelopoulos, V., Harris, C., Artemyev, A., Kepko, L., & Runov, A. (2017). Extensive electron transport and energization via multiple, localized dipolarizing flux bundles. *Journal of Geophysical Research*, *122*(5), 5059–5076. https://doi.org/10.1002/2017JA023981

Gabrielse, C., Angelopoulos, V., Runov, A., & Turner, D. L. (2014). Statistical characteristics of particle injections throughout the equatorial magnetotail. *Journal of Geophysical Research*, *119*(4), 2512–2535. https://doi.org/10.1002/2013JA019638

Gabrielse, C., Spanswick, E., Artemyev, A., Nishimura, Y., Runov, A., Lyons, L., et al. (2019). Utilizing the heliophysics/geospace System observatory to understand particle injections: Their scale sizes and propagation directions. *Journal of Geophysical Research (Space Physics)*, *124*(7), 5584–5609. https://doi.org/10.1029/2018JA025588

Ghaffari, R., Cully, C. M., & Gabrielse, C. (2021). Statistical study of whistler-mode waves and expected pitch angle diffusion rates during dispersionless electron injections. *Geophysical Research Letters*, *48*(17), e2021GL094085. https://doi.org/10.1029/2021GL094085

Ghaffari, R., Cully, C. M., Turner, D. L., & Reeves, G. D. (2020). Characteristics of electron precipitation during 40 energetic electron injections inferred via subionospheric VLF signal propagation. *Journal of Geophysical Research (Space Physics)*, *125*(11), e27233. https://doi.org/10.1029/2019JA027233

Gjerloev, J. W. (2012). The supermag data processing technique. *Journal of Geophysical Research*, *117*(A9). https://doi.org/10.1029/2012JA017683

Graham, D. B., Khotyaintsev, Y. V., Norgren, C., Vaivads, A., André, M., Toledo-Redondo, S., et al. (2017). Lower hybrid waves in the ion diffusion and magnetospheric inflow regions. *Journal of Geophysical Research: Space Physics*, *122*(1), 517–533. https://doi.org/10.1002/2016JA023572

Gurram, H., Egedal, J., & Daughton, W. (2021). Shear Alfvén waves driven by magnetic reconnection as an energy source for the aurora borealis. *Geophysical Research Letters*, *48*(14), e94201. https://doi.org/10.1029/2021GL094201

Hardy, D. A., Schmitt, L. K., Gussenhoven, M. S., Marshall, F. J., & Yeh, H. C. (1984). Precipitating electron and ion detectors (SSJ/4) for the block 5D/Flights 6-10 DMSP (Defense Meteorological Satellite Program) satellites: Calibration and data presentation.

Hargreaves, J. (1969). Auroral absorption of HF radio waves in the ionosphere: A review of results from the first decade of riometry. *Proceedings of the IEEE*, *57*(8), 1348–1373. https://doi.org/10.1109/PROC.1969.7275

Hasegawa, A., & Chen, L. (1975). Kinetic process of plasma heating due to Alfvén wave excitation. *Physical Review Letters*, *35*(6), 370–373. https://doi.org/10.1103/PhysRevLett.35.370

Henderson, M. G. (2012). Auroral substorms, poleward boundary activations, auroral streamers, omega bands, and onset precursor activity. In *Auroral phenomenology and magnetospheric processes: Earth and other planets* (pp. 39–54). American Geophysical Union (AGU). https://doi.org/10.1029/2011GM001165

Jaynes, A. N., Baker, D. N., Singer, H. J., Rodriguez, J. V., Loto'aniu, T. M., Ali, A. F., et al. (2015). Source and seed populations for relativistic electrons: Their roles in radiation belt changes. *Journal of Geophysical Research: Space Physics*, *120*(9), 7240–7254. https://doi.org/10.1002/2015JA021234

Johnson, J. R., & Cheng, C. Z. (2001). Stochastic ion heating at the magnetopause due to kinetic Alfvén waves. *Geophysical Research Letters*, *28*(23), 4421–4424. https://doi.org/10.1029/2001GL013509

Karlsson, T., Andersson, L., Gillies, D. M., Lynch, K., Marghitu, O., Partamies, N., et al. (2020). Quiet, discrete auroral arcs—Observations. *Space Science Reviews*, *216*(1), 16. https://doi.org/10.1007/s11214-020-0641-7

Kataoka, R., Chaston, C., Knudsen, D., Lynch, K., Lysak, R., Song, Y., et al. (2021). Small-scale dynamic Aurora. *Space Science Reviews*, *217*(1), 17. https://doi.org/10.1007/s11214-021-00796-w

Keiling, A. (2009). Alfvén waves and their roles in the dynamics of the Earth's magnetotail: A review. *Space Science Reviews*, *142*(1–4), 73–156. https://doi.org/10.1007/s11214-008-9463-8

Kellerman, A. C., Shprits, Y. Y., Makarevich, R. A., Spanswick, E., Donovan, E., & Reeves, G. (2015). Characterization of the energy-dependent response of riometer absorption. *Journal of Geophysical Research: Space Physics*, *120*(1), 615–631. https://doi.org/10.1002/2014JA020027

Kennel, C. F., & Engelmann, F. (1966). Velocity space diffusion from weak plasma turbulence in a magnetic field. *Physics of Fluids*, *9*(12), 2377–2388. https://doi.org/10.1063/1.1761629

Kennel, C. F., & Petschek, H. E. (1966). Limit on stably trapped particle fluxes. *Journal of Geophysical Research*, *71*, 1–28. https://doi.org/10.1029/jz071i001p00001

Kepko, L., McPherron, R. L., Amm, O., Apatenkov, S., Baumjohann, W., Birn, J., et al. (2014). Substorm current wedge revisited. *Space Science Reviews*, *190*(1–4), 1–46. https://doi.org/10.1007/s11214-014-0124-9

Khazanov, G. V., Robinson, R. M., Zesta, E., Sibeck, D. G., Chu, M., & Grubbs, G. A. (2018). Impact of precipitating electrons and magnetosphere-ionosphere coupling processes on ionospheric conductance. *Space Weather*, *16*(7), 829–837. https://doi.org/10.1029/2018SW001837

Khotyaintsev, Y. V., Cully, C. M., Vaivads, A., André, M., & Owen, C. J. (2011). Plasma jet braking: Energy dissipation and nonadiabatic electrons. *Physical Review Letters*, *106*(16), 165001. https://doi.org/10.1103/PhysRevLett.106.165001

Lam, M. M., Horne, R. B., Meredith, N. P., Glauert, S. A., Moffat-Griffin, T., & Green, J. C. (2010). Origin of energetic electron precipitation ¿30 keV into the atmosphere. *Journal of Geophysical Research: Space Physics*, *115*(8),A00F08. https://doi.org/10.1029/2009JA014619

Le Contel, O., Roux, A., Jacquey, C., Robert, P., Berthomier, M., Chust, T., et al. (2009). Quasi-parallel whistler mode waves observed by THEMIS during near-Earth dipolarizations. *Annales Geophysicae*, *27*(6), 2259–2275. https://doi.org/10.5194/angeo-27-2259-2009

Le Contel, O., Roux, A., Robert, P., Coillot, C., Bouabdellah, A., de La Porte, B., et al. (2008). First results of the THEMIS search coil magnetometers. *Space Science Reviews*, *141*(1–4), 509–534. https://doi.org/10.1007/s11214-008-9371-y

Lejosne, S., & Kollmann, P. (2020). Radiation belt radial diffusion at Earth and beyond. *Space Science Reviews*, *216*(1), 19. https://doi.org/10.1007/s11214-020-0642-6

Li, L., Omura, Y., Zhou, X.-Z., Zong, Q.-G., Rankin, R., Yue, C., & Fu, S.-Y. (2022). Nonlinear wave growth Analysis of chorus emissions modulated by ULF waves. *Geophysical Research Letters*, *49*(10), e97978. https://doi.org/10.1029/2022GL097978

Li, W., Bortnik, J., Thorne, R. M., & Angelopoulos, V. (2011). Global distribution of wave amplitudes and wave normal angles of chorus waves using THEMIS wave observations. *Journal of Geophysical Research*, *116*(A12), 12205. https://doi.org/10.1029/2011JA017035

Li, W., Ni, B., Thorne, R. M., Bortnik, J., Green, J. C., Kletzing, C. A., et al. (2013). Constructing the global distribution of chorus wave intensity using measurements of electrons by the POES satellites and waves by the Van Allen Probes. *Geophysical Research Letters*, *40*(17), 4526–4532. https://doi.org/10.1002/grl.50920

Li, W., Thorne, R. M., Angelopoulos, V., Bonnell, J. W., McFadden, J. P., Carlson, C. W., et al. (2009). Evaluation of whistler-mode chorus intensification on the nightside during an injection event observed on the THEMIS spacecraft. *Journal of Geophysical Research*, *114*(A1). https://doi.org/10.1029/2008JA013554

Li, W., Thorne, R. M., Bortnik, J., Nishimura, Y., & Angelopoulos, V. (2011). Modulation of whistler mode chorus waves: 1. Role of compressional Pc4-5 pulsations. *Journal of Geophysical Research*, *116*(A6), A06205. https://doi.org/10.1029/2010JA016312

Liang, J., Shen, Y., Knudsen, D., Spanswick, E., Burchill, J., & Donovan, E. (2019). E-POP and red line optical observations of Alfvénic auroras. *Journal of Geophysical Research (Space Physics)*, *124*(6), 4672–4696. https://doi.org/10.1029/2019JA026679

Lin, Y., Johnson, J. R., & Wang, X. (2012). Three-dimensional mode conversion associated with kinetic Alfvén waves. *Physical Review Letters*, *109*(12), 125003. https://doi.org/10.1103/PhysRevLett.109.125003

Liu, J., Angelopoulos, V., Runov, A., & Zhou, X.-Z. (2013). On the current sheets surrounding dipolarizing flux bundles in the magnetotail: The case for wedgelets. *Journal of Geophysical Research*, *118*(5), 2000–2020. https://doi.org/10.1002/jgra.50092

Liu, J., Angelopoulos, V., Zhang, X. J., Runov, A., Artemyev, A., Plaschke, F., et al. (2017). Ultralow frequency waves deep inside the inner magnetosphere driven by dipolarizing flux bundles. *Journal of Geophysical Research (Space Physics)*, *122*(10), 10112–10128. https://doi.org/10.1002/2017JA024270

Liu, J., Angelopoulos, V., Zhou, X.-Z., & Runov, A. (2014). Magnetic flux transport by dipolarizing flux bundles. *Journal of Geophysical Research*, *119*(2), 909–926. https://doi.org/10.1002/2013JA019395

Lyons, L. R., Nishimura, Y., Xing, X., Runov, A., Angelopoulos, V., Donovan, E., & Kikuchi, T. (2012). Coupling of dipolarization front flow bursts to substorm expansion phase phenomena within the magnetosphere and ionosphere. *Journal of Geophysical Research*, *117*(A2), 2212. https://doi.org/10.1029/2011JA017265

Lysak, R. L., & Lotko, W. (1996). On the kinetic dispersion relation for shear alfvén waves. *Journal of Geophysical Research*, *101*(A3), 5085–5094. https://doi.org/10.1029/95JA03712

Ma, Q., Li, W., Thorne, R. M., Bortnik, J., Kletzing, C. A., Kurth, W. S., & Hospodarsky, G. B. (2016). Electron scattering by magnetosonic waves in the inner magnetosphere. *Journal of Geophysical Research*, *121*(1), 274–285. https://doi.org/10.1002/2015JA021992

Malaspina, D. M., Wygant, J. R., Ergun, R. E., Reeves, G. D., Skoug, R. M., & Larsen, B. A. (2015). Electric field structures and waves at plasma boundaries in the inner magnetosphere. *Journal of Geophysical Research*, *120*(6), 4246–4263. https://doi.org/10.1002/2015JA021137

Mauk, B. H., Fox, N. J., Kanekal, S. G., Kessel, R. L., Sibeck, D. G., & Ukhorskiy, A. (2013). Science objectives and rationale for the radiation belt Storm Probes Mission. *Space Science Reviews*, *179*(1–4), 3–27. https://doi.org/10.1007/s11214-012-9908-y

McFadden, J. P., Carlson, C. W., Larson, D., Ludlam, M., Abiad, R., Elliott, B., et al. (2008). The THEMIS ESA plasma instrument and in-flight calibration. *Space Science Reviews*, *141*(1–4), 277–302. https://doi.org/10.1007/s11214-008-9440-2

McIlwain, C. E. (1974). Substorm injection boundaries. In B. M. McCormac (Ed.), *Magnetospheric physics* (pp. 143–154).

McPherron, R. L. (1972). Substorm related changes in the geomagnetic tail: The growth phase. *Planatary Space Science*, *20*(9), 1521–1539. https://doi.org/10.1016/0032-0633(72)90054-2

Means, J. D. (1972). Use of the three-dimensional covariance matrix in analyzing the polarization properties of plane waves. *Journal of Geophysical Research*, *77*(28), 5551–5559. https://doi.org/10.1029/JA077i028p05551

Meredith, N. P., Bortnik, J., Horne, R. B., Li, W., & Shen, X.-C. (2021). Statistical investigation of the frequency dependence of the chorus source mechanism of plasmaspheric hiss. *Geophysical Research Letters*, *48*(6), e2021GL092725. https://doi.org/10.1029/2021GL092725

Millan, R. M., & Baker, D. N. (2012). Acceleration of particles to high energies in Earth's radiation belts. *Space Science Reviews*, *173*(1–4), 103–131. https://doi.org/10.1007/s11214-012-9941-x

Millan, R. M., & Thorne, R. M. (2007). Review of radiation belt relativistic electron losses. *Journal of Atmospheric and Solar-Terrestrial Physics*, *69*(3), 362–377. https://doi.org/10.1016/j.jastp.2006.06.019

Mourenas, D., Artemyev, A. V., Agapitov, O. V., & Krasnoselskikh, V. (2013). Analytical estimates of electron quasi-linear diffusion by fast magnetosonic waves. *Journal of Geophysical Research*, *118*(6), 3096–3112. https://doi.org/10.1002/jgra.50349

Mourenas, D., Artemyev, A. V., Ma, Q., Agapitov, O. V., & Li, W. (2016). Fast dropouts of multi-MeV electrons due to combined effects of EMIC and whistler mode waves. *Geophysical Research Letters*, *43*(9), 4155–4163. https://doi.org/10.1002/2016GL068921

Mourenas, D., Artemyev, A. V., Ripoll, J.-F., Agapitov, O. V., & Krasnoselskikh, V. V. (2012). Timescales for electron quasi-linear diffusion by parallel and oblique lower-band Chorus waves. *Journal of Geophysical Research*, *117*(A6), A06234. https://doi.org/10.1029/2012JA017717

Mourenas, D., Artemyev, A. V., Zhang, X. J., Angelopoulos, V., Tsai, E., & Wilkins, C. (2021). Electron lifetimes and diffusion rates inferred from ELFIN measurements at low Altitude: First results. *Journal of Geophysical Research (Space Physics)*, *126*(11), e29757. https://doi.org/10.1029/2021JA029757

Mozer, F. S., Agapitov, O., Artemyev, A., Drake, J. F., Krasnoselskikh, V., Lejosne, S., & Vasko, I. (2015). Time domain structures: What and where they are, what they do, and how they are made. *Geophysical Research Letters*, *42*(10), 3627–3638. https://doi.org/10.1002/2015GL063946

Nakamura, R., Baumjohann, W., Mouikis, C., Kistler, L. M., Runov, A., Volwerk, M., et al. (2004). Spatial scale of high-speed flows in the plasma sheet observed by Cluster. *Geophysical Research Letters*, *31*(9), 9804. https://doi.org/10.1029/2004GL019558

Newell, P. T., & Gjerloev, J. W. (2011). Evaluation of supermag auroral electrojet indices as indicators of substorms and auroral power. *Journal of Geophysical Research*, *116*(A12). https://doi.org/10.1029/2011JA016779

Ni, B., Cao, X., Zou, Z., Zhou, C., Gu, X., Bortnik, J., et al. (2015). Resonant scattering of outer zone relativistic electrons by multiband EMIC waves and resultant electron loss time scales. *Journal of Geophysical Research*, *120*(9), 7357–7373. https://doi.org/10.1002/2015JA021466

Ni, B., Thorne, R. M., & Ma, Q. (2012). Bounce-averaged Fokker-Planck diffusion equation in non-dipolar magnetic fields with applications to the Dungey magnetosphere. *Annales Geophysicae*, *30*(4), 733–750. https://doi.org/10.5194/angeo-30-733-2012

Ni, B., Thorne, R. M., Meredith, N. P., Horne, R. B., & Shprits, Y. Y. (2011). Resonant scattering of plasma sheet electrons leading to diffuse auroral precipitation: 2. Evaluation for whistler mode chorus waves. *Journal of Geophysical Research*, *116*(A4), 4219. https://doi.org/10.1029/2010JA016233

Ni, B., Thorne, R. M., Zhang, X., Bortnik, J., Pu, Z., Xie, L., et al. (2016). Origins of the Earth's diffuse Auroral precipitation. *Space Science Reviews*, *200*(1–4), 205–259. https://doi.org/10.1007/s11214-016-0234-7

Ni, B., Thorne, R. M., Shprits, Y. Y., Orlova, K. G., & Meredith, N. P. (2011). Chorus-driven resonant scattering of diffuse auroral electrons in nondipolar magnetic fields. *Journal of Geophysical Research*, *116*(A6), 6225. https://doi.org/10.1029/2011JA016453

Nishimura, Y., Lessard, M. R., Katoh, Y., Miyoshi, Y., Grono, E., Partamies, N., et al. (2020). Diffuse and Pulsating Aurora. *Space Science Reviews*, *216*(1), 4. https://doi.org/10.1007/s11214-019-0629-3

Nishimura, Y., Lyons, L. R., Angelopoulos, V., Kikuchi, T., Zou, S., & Mende, S. B. (2011). Relations between multiple auroral streamers, pre-onset thin arc formation, and substorm auroral onset. *Journal of Geophysical Research*, *116*(A9), A09214. https://doi.org/10.1029/2011JA016768

Norgren, C., Vaivads, A., Khotyaintsev, Y. V., & André, M. (2012). Lower hybrid drift waves: Space observations. *Physical Review Letters*, *109*(5), 055001. https://doi.org/10.1103/PhysRevLett.109.055001

Panov, E. V., Artemyev, A. V., Baumjohann, W., Nakamura, R., & Angelopoulos, V. (2013). Transient electron precipitation during oscillatory BBF braking: THEMIS observations and theoretical estimates. *Journal of Geophysical Research*, *118*(6), 3065–3076. https://doi.org/10.1002/jgra.50203

Panov, E. V., Nakamura, R., Baumjohann, W., Sergeev, V. A., Petrukovich, A. A., Angelopoulos, V., et al. (2010). Plasma sheet thickness during a bursty bulk flow reversal. *Journal of Geophysical Research*, *115*(A5), A05213. https://doi.org/10.1029/2009JA014743

Paxton, L. J., Morrison, D., Zhang, Y., Kil, H., Wolven, B., Ogorzalek, B. S., et al. (2002). Validation of remote sensing products produced by the Special Sensor Ultraviolet Scanning Imager (SSUSI): A far UV-imaging spectrograph on DMSP F-16. In A. M. Larar & M. G. Mlynczak (Eds.), *Optical spectroscopic techniques, remote sensing, and instrumentation for atmospheric and space research iv* (Vol. 4485, pp. 338–348). https://doi.org/10.1117/12.454268

Reidy, J. A., Horne, R. B., Glauert, S. A., Clilverd, M. A., Meredith, N. P., Woodfield, E. E., et al. (2021). Comparing electron precipitation fluxes calculated from pitch Angle diffusion coefficients to LEO satellite observations. *Journal of Geophysical Research (Space Physics)*, *126*(3), e28410. https://doi.org/10.1029/2020JA028410

Rich, F. J., Hardy, D. A., & Gussenhoven, M. S. (1985). Enhanced ionosphere-magnetosphere data from the DMSP satellites. *EOS Transactions*, *66*(26), 513–514. https://doi.org/10.1029/EO066i026p00513

Runov, A., Angelopoulos, V., Gabrielse, C., Liu, J., Turner, D. L., & Zhou, X.-Z. (2015). Average thermodynamic and spectral properties of plasma in and around dipolarizing flux bundles. *Journal of Geophysical Research*, *120*(6), 4369–4383. https://doi.org/10.1002/2015JA021166

Runov, A., Angelopoulos, V., Gabrielse, C., Zhou, X.-Z., Turner, D., & Plaschke, F. (2013). Electron fluxes and pitch-angle distributions at dipolarization fronts: THEMIS multipoint observations. *Journal of Geophysical Research*, *118*(2), 744–755. https://doi.org/10.1002/jgra.50121

Runov, A., Angelopoulos, V., Sitnov, M. I., Sergeev, V. A., Bonnell, J., McFadden, J. P., et al. (2009). THEMIS observations of an earthward-propagating dipolarization front. *Geophysical Research Letters*, *36*(14), L14106. https://doi.org/10.1029/2009GL038980

Runov, A., Angelopoulos, V., Zhou, X.-Z., Zhang, X.-J., Li, S., Plaschke, F., & Bonnell, J. (2011). A THEMIS multicase study of dipolarization fronts in the magnetotail plasma sheet. *Journal of Geophysical Research*, *116*(A5), 5216. https://doi.org/10.1029/2010JA016316

Runov, A., Sergeev, V. A., Angelopoulos, V., Glassmeier, K.-H., & Singer, H. J. (2014). Diamagnetic oscillations ahead of stopped dipolarization fronts. *Journal of Geophysical Research*, *119*(3), 1643–1657. https://doi.org/10.1002/2013JA019384

Sarafopoulos, D. V., Sidiropoulos, N. F., Sarris, E. T., Lutsenko, V., & Kudela, K. (2001). The dawn-dusk plasma sheet asymmetry of energetic particles: An interball perspective. *Journal of Geophysical Research*, *106*(A7), 13053–13066. https://doi.org/10.1029/2000JA900157

Sarris, E. T., Krimigis, S. M., & Armstrong, T. P. (1976). Observations of magnetospheric bursts of high-energy protons and electrons at approximately 35 Earth radii with Imp 7. *Journal of Geophysical Research*, *81*(13), 2341–2355. https://doi.org/10.1029/JA081i013p02341

Schmid, D., Volwerk, M., Nakamura, R., Baumjohann, W., & Heyn, M. (2011). A statistical and event study of magnetotail dipolarization fronts. *Annales Geophysicae*, *29*(9), 1537–1547. https://doi.org/10.5194/angeo-29-1537-2011

Sergeev, V., Runov, A., Baumjohann, W., Nakamura, R., Zhang, T. L., Volwerk, M., et al. (2003). Current sheet flapping motion and structure observed by Cluster. *Geophysical Research Letters*, *30*(6), 1327. https://doi.org/10.1029/2002GL016500

Sergeev, V. A., Angelopoulos, V., Apatenkov, S., Bonnell, J., Ergun, R., Nakamura, R., et al. (2009). Kinetic structure of the sharp injection/dipolarization front in the flow-braking region. *Geophysical Research Letters*, *36*(21), 21105. https://doi.org/10.1029/2009GL040658

Sergeev, V. A., Gordeev, E. I., Merkin, V. G., & Sitnov, M. I. (2018). Does a local B-minimum appear in the tail current sheet during a substorm growth phase? *Geophysical Research Letters*, *45*(6), 2566–2573. https://doi.org/10.1002/2018GL077183

Sergeev, V. A., Malkov, M., & Mursula, K. (1993). Testing the isotropic boundary algorithm method to evaluate the magnetic field configuration in the tail. *Journal of Geophysical Research*, *98*(A5), 7609–7620. https://doi.org/10.1029/92JA02587

Sergeev, V. A., Nishimura, Y., Kubyshkina, M., Angelopoulos, V., Nakamura, R., & Singer, H. (2012). Magnetospheric location of the equatorward prebreakup arc. *Journal of Geophysical Research: Space Physics*, *117*(A1), A01212. https://doi.org/10.1029/2011JA017154

Sergeev, V. A., Sazhina, E. M., Tsyganenko, N. A., Lundblad, J. A., & Soraas, F. (1983). Pitch-angle scattering of energetic protons in the magnetotail current sheet as the dominant source of their isotropic precipitation into the nightside ionosphere. *Planatary Space Science*, *31*(10), 1147–1155. https://doi.org/10.1016/0032-0633(83)90103-4

Sergeev, V. A., & Tsyganenko, N. A. (1982). Energetic particle losses and trapping boundaries as deduced from calculations with a realistic magnetic field model. *Planatary Space Science*, *30*(10), 999–1006. https://doi.org/10.1016/0032-0633(82)90149-0

Shapiro, V. D., & Sagdeev, R. Z. (1997). Nonlinear wave-particle interaction and conditions for the applicability of quasilinear theory. *Physics Reports*, *283*(1–4), 49–71. https://doi.org/10.1016/S0370-1573(96)00053-1

Sharma Pyakurel, P., Shay, M. A., Haggerty, C. C., Parashar, T. N., Drake, J. F., Cassak, P. A., & Gary, S. P. (2018). Super-Alfvénic propagation and damping of reconnection onset signatures. *Journal of Geophysical Research: Space Physics*, *123*(1), 341–349. https://doi.org/10.1002/2017JA024606

Shen, Y., Artemyev, A., Vasko, I., Zhang, X.-J., Angelopoulos, V., An, X., & Runov, A. (2022a). Energetic electron scattering by kinetic Alfvén waves at strong magnetic field gradients of dipolarization front. *Physics of Plasmas*, *29*(8), 082901. https://doi.org/10.1063/5.0096338

Shen, Y., Artemyev, A., Zhang, X.-J., Vasko, I. Y., Runov, A., Angelopoulos, V., & Knudsen, D. (2020). Potential evidence of low-energy electron scattering and ionospheric precipitation by time domain structures. *Geophysical Research Letters*, *47*(16), e89138. https://doi.org/10.1029/2020GL089138

Shen, Y., Artemyev, A. V., Ma, Q., Zhang, X.-J., Mourenas, D., Tsai, E., et al. (2022b). Inner belt wisp precipitation measured by elfin: Regimes of energetic electron scattering by vlf transmitter waves. *Journal of Geophysical Research: Space Physics*, *127*(11), e2022JA030968. https://doi.org/10.1029/2022JA030968

Shen, Y., Artemyev, A. V., Zhang, X.-J., Angelopoulos, V., Vasko, I., Turner, D., et al. (2022c). Tens to hundreds of keV electron precipitation driven by kinetic Alfvén waves during an electron injection. *Journal of Geophysical Research (Space Physics)*, *127*(8), e30360. https://doi.org/10.1029/2022JA030360

Shen, Y., Vasko, I. Y., Artemyev, A., Malaspina, D. M., Chu, X., Angelopoulos, V., & Zhang, X.-J. (2021). Realistic electron diffusion rates and lifetimes due to scattering by electron holes. *Journal of Geophysical Research (Space Physics)*, *126*(9), e29380. https://doi.org/10.1029/2021JA029380

Shiokawa, K., Baumjohann, W., & Haerendel, G. (1997). Braking of high-speed flows in the near-Earth tail. *Geophysical Research Letters*, *24*(10), 1179–1182. https://doi.org/10.1029/97GL01062

Shprits, Y. Y., Subbotin, D. A., Meredith, N. P., & Elkington, S. R. (2008). Review of modeling of losses and sources of relativistic electrons in the outer radiation belt II: Local acceleration and loss. *Journal of Atmospheric and Solar-Terrestrial Physics*, *70*(14), 1694–1713. https://doi.org/10.1016/j.jastp.2008.06.014

Shprits, Y. Y., Thorne, R. M., Horne, R. B., & Summers, D. (2006). Bounce-averaged diffusion coefficients for field-aligned chorus waves. *Journal of Geophysical Research*, *111*(A10), 10225. https://doi.org/10.1029/2006JA011725

Sitnov, M. I., Birn, J., Ferdousi, B., Gordeev, E., Khotyaintsev, Y., Merkin, V., et al. (2019). Explosive magnetotail Activity. *Space Science Reviews*, *215*(4), 31. https://doi.org/10.1007/s11214-019-0599-5

Sorathia, K. A., Ukhorskiy, A. Y., Merkin, V. G., Fennell, J. F., & Claudepierre, S. G. (2018). Modeling the depletion and recovery of the outer radiation belt during a geomagnetic Storm: Combined MHD and test particle simulations. *Journal of Geophysical Research: Space Physics*, *123*(7), 5590–5609. https://doi.org/10.1029/2018JA025506

Sotirelis, T., Korth, H., Hsieh, S.-Y., Zhang, Y., Morrison, D., & Paxton, L. (2013). Empirical relationship between electron precipitation and far-ultraviolet auroral emissions from DMSP observations. *Journal of Geophysical Research: Space Physics*, *118*(3), 1203–1209. https://doi.org/10.1002/jgra.50157

Spanswick, E., Donovan, E., Friedel, R., & Korth, A. (2007). Ground based identification of dispersionless electron injections. *Geophysical Research Letters*, *34*(3), L03101. https://doi.org/10.1029/2006GL028329

Spanswick, E., Reeves, G. D., Donovan, E., & Friedel, R. H. W. (2010). Injection region propagation outside of geosynchronous orbit. *Journal of Geophysical Research*, *115*(A11), 11214. https://doi.org/10.1029/2009JA015066

Stasiewicz, K., Bellan, P., Chaston, C., Kletzing, C., Lysak, R., Maggs, J., et al. (2000). Small scale Alfvénic structure in the aurora. *Space Science Reviews*, *92*(3/4), 423–533. https://doi.org/10.1023/a:1005207202143

Summers, D. (2005). Quasi-linear diffusion coefficients for field-aligned electromagnetic waves with applications to the magnetosphere. *Journal of Geophysical Research*, *110*(A8), 8213. https://doi.org/10.1029/2005JA011159

Summers, D., Ni, B., & Meredith, N. P. (2007). Timescales for radiation belt electron acceleration and loss due to resonant wave-particle interactions: 2. Evaluation for VLF chorus, ELF hiss, and electromagnetic ion cyclotron waves. *Journal of Geophysical Research*, *112*(A4), 4207. https://doi.org/10.1029/2006JA011993

Summers, D., & Thorne, R. M. (2003). Relativistic electron pitch-angle scattering by electromagnetic ion cyclotron waves during geomagnetic storms. *Journal of Geophysical Research*, *108*(A4), 1143. https://doi.org/10.1029/2002JA009489

Thorne, R. M. (2010). Radiation belt dynamics: The importance of wave-particle interactions. *Geophysical Research Letters*, *372*(22), 22107. https://doi.org/10.1029/2010GL044990

Thorne, R. M., Bortnik, J., Li, W., & Ma, Q. (2021). Wave–particle interactions in the Earth's magnetosphere. In *Magnetospheres in the solar system* (pp. 93–108). American Geophysical Union (AGU). https://doi.org/10.1002/9781119815624.ch6

Thorne, R. M., Ni, B., Tao, X., Horne, R. B., & Meredith, N. P. (2010). Scattering by chorus waves as the dominant cause of diffuse auroral precipitation. *Nature*, *467*(7318), 943–946. https://doi.org/10.1038/nature09467

Tsurutani, B. T., & Smith, E. J. (1974). Postmidnight chorus: A substorm phenomenon. *Journal of Geophysical Research*, *79*(1), 118–127. https://doi.org/10.1029/JA079i001p00118

Tsyganenko, N. A. (2002). A model of the near magnetosphere with a dawn-dusk asymmetry 1. Mathematical structure. *Journal of Geophysical Research.*, *107*(A8), 1179. https://doi.org/10.1029/2001JA000219

Turner, D. L., Fennell, J. F., Blake, J. B., Clemmons, J. H., Mauk, B. H., Cohen, I. J., et al. (2016). Energy limits of electron acceleration in the plasma sheet during substorms: A case study with the magnetospheric multiscale (mms) mission. *Geophysical Research Letters*, *43*(15), 7785–7794. https://doi.org/10.1002/2016GL069691

Ukhorskiy, A. Y., & Sitnov, M. I. (2013). Dynamics of radiation belt particles. *Space Science Reviews*, *179*(1–4), 545–578. https://doi.org/10.1007/s11214-012-9938-5

Ukhorskiy, A. Y., Sitnov, M. I., Millan, R. M., & Kress, B. T. (2011). The role of drift orbit bifurcations in energization and loss of electrons in the outer radiation belt. *Journal of Geophysical Research*, *116*(A9), 9208. https://doi.org/10.1029/2011JA016623

Ukhorskiy, A. Y., Sorathia, K. A., Merkin, V. G., Crabtree, C., Fletcher, A. C., Malaspina, D. M., & Schwartz, S. J. (2022). Cross-scale energy cascade powered by magnetospheric convection. *Scientific Reports*, *12*(1), 4446. https://doi.org/10.1038/s41598-022-08038-x

Usanova, M. E., & Ergun, R. E. (2022). Electron energization by high-Amplitude turbulent electric fields: A possible source of the outer radiation belt. *Journal of Geophysical Research (Space Physics)*, *127*(7), e30336. https://doi.org/10.1029/2022JA030336

Vasko, I. Y., Agapitov, O. V., Mozer, F. S., Artemyev, A. V., Krasnoselskikh, V. V., & Bonnell, J. W. (2017). Diffusive scattering of electrons by electron holes around injection fronts. *Journal of Geophysical Research*, *122*(3), 3163–3182. https://doi.org/10.1002/2016JA023337

Vasko, I. Y., Krasnoselskikh, V. V., Mozer, F. S., & Artemyev, A. V. (2018). Scattering by the broadband electrostatic turbulence in the space plasma. *Physics of Plasmas*, *25*(7), 072903. https://doi.org/10.1063/1.5039687

Viberg, H., Khotyaintsev, Y. V., Vaivads, A., André, M., Fu, H. S., & Cornilleau-Wehrlin, N. (2014). Whistler mode waves at magnetotail dipolarization fronts. *Journal of Geophysical Research*, *119*(4), 2605–2611. https://doi.org/10.1002/2014JA019892

Wang, G., Su, Z., Zheng, H., Wang, Y., Zhang, M., & Wang, S. (2017). Nonlinear fundamental and harmonic cyclotron resonant scattering of radiation belt ultrarelativistic electrons by oblique monochromatic emic waves. *Journal of Geophysical Research*, *122*(2), 1928–1945. https://doi.org/10.1002/2016JA023451

Watt, C. E. J., & Rankin, R. (2009). Electron trapping in shear Alfvén waves that power the aurora. *Physical Review Letters*, *102*(4), 045002. https://doi.org/10.1103/PhysRevLett.102.045002

Wygant, J. R., Keiling, A., Cattell, C. A., Lysak, R. L., Temerin, M., Mozer, F. S., et al. (2002). Evidence for kinetic Alfvén waves and parallel electron energization at 4-6 RE altitudes in the plasma she$_e$t boundary layer. *Journal of Geophysical Research*, *107*(A8), 1201. https://doi.org/10.1029/2001JA900113

Xia, Z., Chen, L., Dai, L., Claudepierre, S. G., Chan, A. A., Soto-Chavez, A. R., & Reeves, G. D. (2016). Modulation of chorus intensity by ULF waves deep in the inner magnetosphere. *Geophysical Research Letters*, *43*(18), 9444–9452. https://doi.org/10.1002/2016GL070280

Zhang, X., & Angelopoulos, V. (2014). On the relationship of electrostatic cyclotron harmonic emissions with electron injections and dipolarization fronts. *Journal of Geophysical Research*, *119*(4), 2536–2549. https://doi.org/10.1002/2013JA019540

Zhang, X., Angelopoulos, V., Artemyev, A. V., & Liu, J. (2018). Whistler and electron firehose instability control of electron distributions in and Around dipolarizing flux bundles. *Geophysical Research Letters*, *45*(18), 9380–9389. https://doi.org/10.1029/2018GL079613

Zhang, X., Angelopoulos, V., Artemyev, A. V., & Liu, J. (2019). Energy transport by whistler waves around dipolarizing flux bundles. *Geophysical Research Letters*, *46*(21), 11718–11727. https://doi.org/10.1029/2019GL084226

Zhang, X., Angelopoulos, V., Ni, B., Thorne, R. M., & Horne, R. B. (2014). Extent of ECH wave emissions in the Earth's magnetotail. *Journal of Geophysical Research*, *119*(7), 5561–5574. https://doi.org/10.1002/2014JA019931

Zhang, X. J., Angelopoulos, V., Artemyev, A. V., Hartinger, M. D., & Bortnik, J. (2020). Modulation of whistler waves by ultra-low-frequency perturbations: The importance of magnetopause location. *Journal of Geophysical Research (Space Physics)*, *125*(10), e28334. https://doi.org/10.1029/2020JA028334

Zhang, X.-J., Angelopoulos, V., Ni, B., & Thorne, R. M. (2015). Predominance of ECH wave contribution to diffuse aurora in Earth's outer magnetosphere. *Journal of Geophysical Research*, *120*(1), 295–309. https://doi.org/10.1002/2014JA020455

Zhang, X.-J., Chen, L., Artemyev, A. V., Angelopoulos, V., & Liu, X. (2019). Periodic excitation of chorus and ECH waves modulated by ultra-low frequency compressions. *Journal of Geophysical Research (Space Physics)*, *124*(11), 8535–8550. https://doi.org/10.1029/2019JA027201

Zhou, M., Deng, X. H., Li, S. Y., Pang, Y., Vaivads, A., Rème, H., et al. (2009). Observation of waves near lower hybrid frequency in the reconnection region with thin current sheet. *Journal of Geophysical Research*, *114*(A2), 2216. https://doi.org/10.1029/2008JA013427

Zhou, M., Ni, B., Huang, S., Deng, X., Ashour-Abdalla, M., Nishimura, Y., et al. (2014). Observation of large-amplitude magnetosonic waves at dipolarization fronts. *Journal of Geophysical Research*, *119*(6), 4335–4347. https://doi.org/10.1002/2014JA019796

Zhou, X., Angelopoulos, V., Sergeev, V. A., & Runov, A. (2010). Accelerated ions ahead of earthward propagating dipolarization fronts. *Journal of Geophysical Research*, *115*(A5), A00I03. https://doi.org/10.1029/2010JA015481